

Galaxy-wide radio-induced feedback in a radio-quiet quasar

M. Villar-Martín,^{1,2★} B. Emonts,^{1,2} A. Cabrera Lavers,^{3,4} C. Tadhunter,⁵
 D. Mukherjee,⁶ A. Humphrey,⁷ J. Rodríguez Zaurín,⁵ C. Ramos Almeida,^{4,8}
 M. Pérez Torres^{9,10} and P. Bessiere¹¹

¹Centro de Astrobiología (INTA-CSIC), Carretera de Ajalvir, km 4, Torrejón de Ardoz, E-28850 Madrid, Spain

²Astro-UAM, UAM, Unidad Asociada CSIC, Facultad de Ciencias, Campus de Cantoblanco, E-28049 Madrid, Spain

³GRANTECAN, Cuesta de San José s/n, E-38712 Breña Baja, La Palma, Spain

⁴Instituto de Astrofísica de Canarias, Vía Láctea s/n, E-38200 La Laguna, Tenerife, Spain

⁵Department of Physics and Astronomy, University of Sheffield, Sheffield S3 7RH, UK

⁶Research School of Astronomy and Astrophysics, Australian National University, Canberra, ACT 2611, Australia

⁷Instituto de Astrofísica e Ciências do Espaço, Universidade do Porto, CAUP, Rua das Estrelas, P4150-762 Porto, Portugal

⁸Departamento de Astrofísica, Universidad de La Laguna (ULL), E-38205 La Laguna, Tenerife, Spain

⁹Instituto de Astrofísica de Andalucía (IAA-CSIC), Apdo. 3004, E-18080 Granada, Spain

¹⁰Departamento de Física Teórica, Universidad de Zaragoza, C/Pedro Cerbuna 12, E-50009 Zaragoza, Spain

¹¹Facultad de Física, Instituto de Astrofísica, Pontificia Universidad Católica de Chile, Casilla 306, Santiago 22, Chile

Accepted 2017 August 24. Received 2017 August 24; in original form 2017 May 5

ABSTRACT

We report the discovery of a radio-quiet type 2 quasar (SDSS J165315.06+234943.0 nicknamed the ‘Beetle’ at $z = 0.103$) with unambiguous evidence for active galactic nucleus (AGN) radio-induced feedback acting across a total extension of ~ 46 kpc and up to ~ 26 kpc from the AGN. To the best of our knowledge, this is the first radio-quiet system where radio-induced feedback has been securely identified at \gg several kpc from the AGN. The morphological, ionization and kinematic properties of the extended ionized gas are correlated with the radio structures. We find along the radio axis (a) enhancement of the optical line emission at the location of the radio hotspots (b) turbulent gas kinematics ($\text{FWHM} \sim 380\text{--}470 \text{ km s}^{-1}$) across the entire spatial range circumscribed by them (c) ionization minima for the turbulent gas at the location of the hot spots, (d) high temperature $T_e \gtrsim 1.9 \times 10^4 \text{ K}$ at the NE hotspot. Turbulent gas is also found far from the radio axis, ~ 25 kpc in the perpendicular direction. We propose a scenario in which the radio structures have perforated the interstellar medium of the galaxy and escaped into the circumgalactic medium. While advancing, they have interacted with *in situ* gas modifying its properties. Our results show that jets of modest power can be the dominant feedback mechanism acting across huge volumes in radio-quiet systems, including highly accreting luminous AGNs, where radiative mode feedback may be expected.

Key words: galaxies: active – galaxies: evolution – quasars: individual: SDSS J1653+23.

1 INTRODUCTION

Feedback induced by the activity of supermassive black holes (SMBH) in massive galaxies is thought to play a critical role in their evolution by means of regulating the amount of gas available for star formation and black hole growth. This type of active galactic nucleus (AGN) feedback refers to the processes of interaction between the energy and radiation generated by accretion on to the massive black hole and the gas in the host galaxy (Fabian 2012). This may give answers to some fundamental questions in cosmology

(Silk & Rees 1998; King 2003; Silk & Rees 2012), such as the discrepancy between the predicted and observed high-mass end of the galaxy luminosity function and the observed correlations between the black hole mass and some properties of the spheroidal component in galaxies (Ferrarese & Merritt 2000; McConnell & Ma 2013). Hydrodynamic simulations show that the energy output of these outflows can indeed regulate the growth and activity of black holes and their host galaxies (Di Matteo, Springel & Hernquist 2005). For this, the intense flux of photons and particles produced by the AGN must sweep the galaxy clean of interstellar gas and terminate star formation and the activity of the SMBH (Fabian 2012). The most powerful outflows with potentially the most extreme effects on the environment are expected in quasars, the most powerful AGN

* E-mail: villarmm@cab.inta-csic.es

(Page et al. 2012; Woo, Son & Bae 2017). Observational evidence for such a dramatic impact is however controversial.

Since their recent discovery, optically selected type 2 quasars (QSO2, Zakamska et al. 2003; Reyes et al. 2008) have been unique systems for investigating the way feedback works in the most powerful AGN. The active nucleus is obscured and this allows a detailed study of many properties of the surrounding medium without the overwhelming glare of the quasar, which strongly affects related studies of their unobscured type 1 counterparts (QSO1).

During recent years, it has become clear that ionized outflows are ubiquitous in QSO2 at different z (Greene et al. 2011; Villar Martín et al. 2011, 2016; Harrison et al. 2012; Liu et al. 2013; Förster Schreiber et al. 2014; Harrison et al. 2014; McElroy et al. 2015). Extreme motions are often measured, with FWHM $> 1000 \text{ km s}^{-1}$ and typical velocity shifts $V_S \sim \text{several} \times 100 \text{ km s}^{-1}$. The outflows are triggered by AGN-related processes (e.g. Villar Martín 2014, hereafter VM14; Zakamska & Greene 2014).

The case for effective gas ejection and star formation truncation exerted by the ionized outflows is less clear. Recent integral field spectroscopic studies of QSO2 at $z \lesssim 0.7$ have suggested that large-scale, wide angle AGN-driven ionized outflows are prevalent in these systems and their action can be exerted across many kpc, even the entire galaxy (Liu et al. 2013; Harrison et al. 2014; McElroy et al. 2015). The kinetic energies, \dot{E}_o , outflow masses, M_o and mass outflow rates, \dot{M}_o , are estimated to be large enough for a significant impact on their hosts. In the proposed scenario, processes related to the accretion disc (thermal, radiation and magnetic driving) launch a relativistic wide angle wind that then shocks the surrounding gas and drives the outflow (e.g. Proga 2007; Zubovas & King 2014). On the other hand, the above observational results have been questioned by different authors (VM14; Husemann et al. 2016; Karouzos, Woo & Bae 2016; Villar Martín et al. 2016; see also Husemann et al. 2013 for QSO1) who find that the ionized outflows are constrained in general within $R_o \lesssim 1\text{--}2 \text{ kpc}$. This raises doubts about their impact on the host galaxies, since their effectiveness as a feedback mechanism would be significantly reduced.

Another mechanism of AGN feedback is that induced by relativistic jets. The jets originate in the vicinity of the SMBH, on scales of a few to 100 times the gravitational radius. Three-dimensional relativistic hydrodynamic simulations of interactions of AGN jets with a dense turbulent two-phase interstellar medium (ISM) show that the originally well-directed jets form an energy-driven almost spherical bubble that can affect the gas to distances up to several kpc from the injection region, depending on the jet power. The shocks resulting from such interactions create a multiphase ISM and radial outflows (e.g. Mukherjee et al. 2016).

Observational studies of powerful radio galaxies and radio-loud QSO1 at different z show that the interaction between the radio structures and the ambient gas can indeed induce outflows that can extend across many kpc, sometimes well outside the galaxy boundaries (Tadhunter et al. 1994; McCarthy, Baum & Spinrad 1996; Villar Martín et al. 1999, 2003; Solórzano-Iñarrea, Tadhunter & Axon 2002; Humphrey et al. 2006; Fu & Stockton 2009). They may have enormous energies sufficient to eject a large fraction of the gaseous content out of the galaxy and/or quench star formation, thus having an important impact on the evolution of the host galaxies (Morganti, Tadhunter & Oosterloo 2005; Nesvadba et al. 2006; Nesvadba et al. 2008).

This feedback mechanism (hereafter radio-induced feedback) has been proposed to explain the gas cooling problem at the centre of

galaxy clusters (see Fabian 2012 for a review). It may also prevent the formation of extremely bright galaxies at the centre of clusters (e.g. Sijacki & Springel 2006). Such scenarios involve a central dominant elliptical of a cluster going through a powerful radio-loud phase. Simulations by Gaspari, Brighenti & Temi (2012) show that the radio-induced feedback can have significant effects also in more modest environments, including isolated ellipticals. It could explain the evidence for reduced cooling also in elliptical galaxies and the related absence of cold gas in these systems (Mathews & Baker 1971; Best et al. 2006).

The role of the radio-induced feedback has not been sufficiently explored in the radio-quiet quasars. Only $\sim 15 \pm 5$ per cent of QSO2 are thought to be radio loud (Lal & Ho 2010). The same percentage applies to QSO1 (Kellermann et al. 1994). However, this does not discard radio-induced outflows as a potentially significant feedback mechanism. Radio-gas interactions¹ and the associated outflows have been observed in radio-quiet AGNs for several decades (e.g. Wilson & Ulvestad 1983; Whittle 1985, 1992b). The most extreme ionized outflows are often found in objects (including QSO2) with some degree of radio activity, even if they are not radio loud (e.g. Husemann et al. 2013, 2016; Mullaney et al. 2013; VM14; Zakamska & Greene 2014). Its significant role as a feedback mechanism has been quantified in several low-luminosity AGNs (Seyfert galaxies; Tadhunter et al. 2014; Alatalo et al. 2015). Although the effects are obvious in a small region ($R \lesssim 1 \text{ kpc}$ from the SMBH), the outflows can disturb and heat the molecular gas, thus having the potential to quench star formation (Guillard et al. 2012).

Large-scale effects (\gg several kpc) due to the radio-induced feedback in radio-quiet AGNs are usually not expected, nor are they usually observed. Traditionally, it is assumed that radio-quiet AGNs contain low power jets that will decelerate and lose their power after a few kpc. However, different results suggest that the radio-induced feedback may indeed occur across many kpc in some systems. On one hand, radio-gas interaction simulations show that while a high power jet ($P_{\text{jet}} \gtrsim 10^{45} \text{ erg s}^{-1}$) can remain relativistic to large scales and drill with relative ease through tens of kpc, a jet with low mechanical power ($P_{\text{jet}} \lesssim 10^{43} \text{ erg s}^{-1}$), although less efficient in accelerating clouds, is trapped in the ISM for a longer time and hence can affect the ISM over a larger volume (Bicknell 1994; Mukherjee et al. 2016). On the other hand, some radio-quiet quasars associated with modest or low power jets show large radio sources with sizes in the range of tens or even hundreds of kpc (Kellermann et al. 1994). Thus, it is clear that these radio sources can escape the galaxy boundaries and expand into the circumgalactic medium (CGM).²

However, to the best of our knowledge, the effects of radio-gas interactions have not been directly observed beyond scales of \sim several kpc from the AGN in such systems. The ‘Teacup’ QSO2 ($z = 0.085$), which shows $\sim 10\text{--}12 \text{ kpc}$ radio/optical bubbles, may be the radio-quiet AGN where the effects of radio-gas interactions have been identified across the largest spatial scale so far (Harrison et al. 2015; Ramos Ramos Almeida et al. 2017). It is not clear, however, whether the bubbles have been inflated instead by a wide angle large-scale AGN-driven wind (Harrison et al. 2015).

We report here unambiguous evidence for the radio-induced feedback working across a total extension of $\sim 46 \text{ kpc}$ and up to $\sim 26 \text{ kpc}$ from the AGN, well into the CGM, in a radio-quiet QSO2.

¹ By ‘radio-gas interactions’, we will refer to the interactions between any AGN-related radio structure (jets, lobes, hotspots) and the ambient gas.

² Following Tumilson et al. (2017), we consider the CGM as the gas surrounding galaxies outside their discs or ISM and inside their virial radii.

We present a detailed study of SDSS J165315.06+234943.0 (nicknamed the ‘Beetle’ hereafter) at $z = 0.103$ based on Gran Telescopio Canarias (GTC) optical images and long-slit spectroscopy and Very Large Array (VLA) radio maps. The data reveal that the radio-induced feedback is modifying the morphological, kinematic and physical properties of the gaseous environment on scales from (possibly) ~ 1 kpc up to the CGM.

Previous knowledge on the ‘Beetle’ is summarized in Section 1.1. The observations, reduction and analysis methods of the different data sets (optical imaging and spectroscopy, radio maps) are described in Section 2. Analysis and results are presented in Section 3 and discussed in Section 4. The summary and conclusions are in Section 5.

We adopt $H_0 = 71 \text{ km s}^{-1} \text{ Mpc}^{-1}$, $\Omega_\Lambda = 0.73$ and $\Omega_m = 0.27$. This gives an arcsec to kpc conversion of $1.87 \text{ kpc arcsec}^{-1}$ at $z = 0.103$.

1.1 The radio-quiet QSO2 SDSS J165315.06+234943.0

The ‘Beetle’ was originally selected by Reyes et al. (2008) for their Sloan Digital Sky Survey (SDSS; York et al. 2000) catalogue of optically selected QSO2 at $z \lesssim 0.8$. Its [O III] $\lambda 5007$ luminosity, $\log(L_{[\text{O III}]}) = 42.6$, corresponds to a bolometric luminosity $\log(L_{\text{bol}}) \sim 46.0$ (Stern & Laor 2012), in the range of quasars (Woo & Urry 2002).

The information and calculations that follow are provided because they will be relevant in later sections.

(i) *Radio loudness.* The ‘Beetle’ has been detected at 1.4 GHz in the VLA Faint Images of the Radio Sky at Twenty-Centimeters (FIRST) survey with a peak flux of 6.4 mJy, while its peak flux in the VLA NRAO VLA Sky Survey (NVSS) is 9.4 mJy. In order to classify this QSO2 according to the radio loudness, we have used the rest-frame radio power at 5 GHz $P_{5 \text{ GHz}}$ and $\log(L_{[\text{O III}]})$ (see fig. 7 in Lal & Ho 2010; see also Xu, Livio & Baum 1999). These two luminosities separate objects clearly into the two families of radio-loud and radio-quiet AGNs with a significant gap between them (Fig. 1). We calculate $P_{5 \text{ GHz}} = 4\pi D_L^2 S_{5 \text{ GHz}}(1+z)^{-1-\alpha}$, where D_L is the luminosity distance, $S_{5 \text{ GHz}}$ is the observed flux density at 5 GHz and α is the spectral index such that $S_\nu \propto \nu^\alpha$. We compute $S_{5 \text{ GHz}}$ from the available $S_{1.4 \text{ GHz}}$. The index α is unknown. For $\alpha = +0.094$ (Lal & Ho 2010), $\log(P_{5 \text{ GHz}}) = 30.4 \text{ (erg s}^{-1} \text{ Hz}^{-1})$. Considering the range $-1.1 \leq \alpha \leq +0.85$ spanned by QSO2s (Lal & Ho 2010), we obtain $\log(P_{5 \text{ GHz}}) = 30.4^{+0.4}_{-0.6} \text{ erg s}^{-1} \text{ Hz}^{-1}$. Fig. 1 shows that the ‘Beetle’ is a radio-quiet QSO2, and this conclusion is not affected by the uncertainty in α .

(ii) *Infrared luminosity and its origin.* The IRAS fluxes for the ‘Beetle’ are $S_{12 \mu\text{m}} = 0.10$, $S_{25 \mu\text{m}} = 0.15$, $S_{60 \mu\text{m}} = 0.49$ and $S_{100 \mu\text{m}} \lesssim 1.01$ Jy. Following Sanders & Mirabel (1996), the total infrared luminosity is $4.3 \times 10^{11} L_\odot < L_{\text{IR}(8-1000 \mu\text{m})} \lesssim 5.5 \times 10^{11} L_\odot^3$ implying that the object is in the regime of luminous infrared galaxies (LIRGs; $10^{11} \leq L_{\text{IR}}/L_\odot < 10^{12}$). Assuming $S_{60 \mu\text{m}}/S_{100 \mu\text{m}} \geq 1.4$ as observed in LIRGs (e.g. Lu et al. 2014; Pearson et al. 2016) then $L_{\text{IR}(8-1000 \mu\text{m})} = (5.0 \pm 0.4) \times 10^{11} L_\odot$. The far-infrared luminosity is $L_{\text{FIR}(40-500 \mu\text{m})} = (1.7 \pm 0.3) \times 10^{11} L_\odot$. If L_{IR} were to be dominated by a starburst contribution, this would imply a star-forming rate $\text{SFR} = 87 \pm 7 M_\odot \text{ yr}^{-1}$ (Kennicutt 1998). However, this is a gross upper limit since L_{IR} is contaminated (maybe dominated) by AGN-heated dust. This is based on

³ k -correction is negligible for $z = 0.103$.

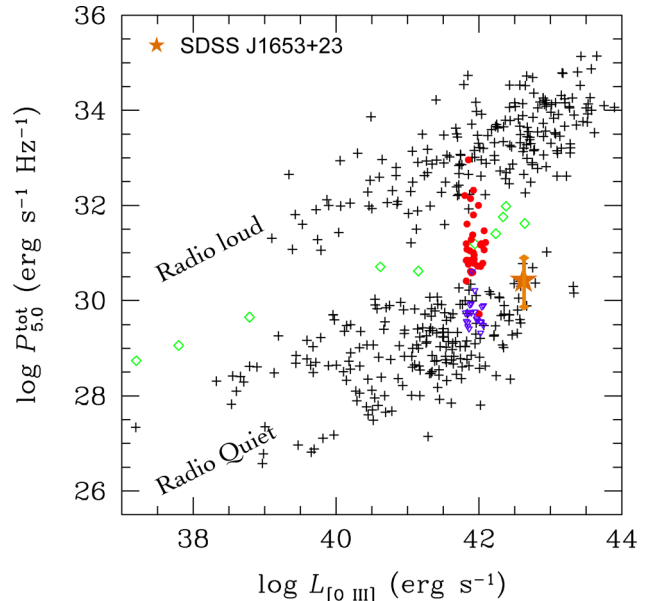


Figure 1. Classification of the ‘Beetle’ according to its radio loudness. The figure is the same as fig. 7 in Lal & Ho (2010) with the location of our object shown as a beige star. The error-bar accounts for the uncertainty in the radio spectral index α . The plus symbols come from the AGN sample of Xu et al. (1999), with the open green diamonds representing their radio intermediate sources. The Lal & Ho (2010) samples of QSO2 at $0.3 \lesssim z \lesssim 0.7$ are represented by filled red circles, with upper limits marked with open blue triangles. The ‘Beetle’ QSO2 is radio quiet. [A colour version of this figure is available in the online version.]

two arguments. Following Helou et al. (1985), we have calculated $q = \log\left[\frac{F_{\text{FIR}/(3.75 \times 10^{12} \text{ Hz})}}{S_{1.4 \text{ GHz}}}\right] = 1.87 \pm 0.09$, where F_{FIR} is the far-infrared flux in $\text{erg s}^{-1} \text{ cm}^{-2}$ and $S_{1.4 \text{ GHz}}$ is in units of $\text{erg s}^{-1} \text{ cm}^{-2} \text{ Hz}^{-1}$. For the ‘Beetle’ q is within the range measured for radio emitting AGNs ($\langle q_{\text{AGN}} \rangle = 2.0$ with rms scatter $\sigma_{\text{AGN}} = 0.59$) and outside the range measured for star-forming galaxies ($\langle q_{\text{SF}} \rangle = 2.3$ with rms scatter $\sigma_{\text{AGN}} = 0.18$). The IR colour $\alpha_{\text{IR}} = \log(S_{25 \mu\text{m}}/S_{60 \mu\text{m}})/\log(60/25) = -1.3$ is also consistent with AGN values ($\alpha_{\text{IR}} > -1.5$, in comparison with $\alpha_{\text{IR}} < -1.5$ for star-forming galaxies; Mauch & Sadler 2007).

(iii) *Stellar velocity dispersion and stellar mass.* Two components of the Mg I triplet at 5169 and 5185 Å are clearly detected in the nuclear GTC spectrum. They have $\sigma = 210 \pm 25 \text{ km s}^{-1}$ and $220 \pm 33 \text{ km s}^{-1}$, respectively, which is in reasonable agreement with $\sigma_* = 169 \pm 8 \text{ km s}^{-1}$ provided by the SDSS Data Release 10 (DR10) kinematic fits. We will assume $\sigma_* \sim 200 \text{ km s}^{-1}$.

Estimated stellar masses for the ‘Beetle’ are in the range $10.64 \lesssim \log\left(\frac{M_*}{M_\odot}\right) \lesssim 11.34$, with a median value 11.2. The different values have been retrieved from the SDSS DR10 and the Vizier catalogue (Ochsenbein, Bauer & Marcout 2000) based on Mendel et al. (2014). According to these authors (see also Simard et al. 2011), the spheroidal component contains a mass $\log(M_{\text{sph}}/M_\odot) = 11.0$.

(iv) *Black hole mass and Eddington luminosity.* We have constrained the black hole mass M_{BH} using the correlation between stellar velocity dispersion σ_* and M_{BH} for early-type galaxies (McConnell & Ma 2013): $\log(M_{\text{BH}}/M_\odot) = 8.39 + 5.20 \log(\sigma_*/200 \text{ km s}^{-1}) = 8.4$, where $\sigma_* \sim 200 \text{ km s}^{-1}$. This is consistent with the value $\log(M_{\text{BH}}/M_\odot) = 8.5$ obtained from the M_{BH} versus bulge (or spheroidal component) mass M_{sph} correlation $\log(M_{\text{BH}}/M_\odot) = 8.46 + 1.05 \log(M_{\text{sph}}/10^{11} M_\odot)$. The

implied Eddington luminosity is $L_{\text{Edd}} = 1.26 \times 10^{38} (M_{\text{BH}}/M_{\odot}) \text{ erg s}^{-1} \sim 3.2 \times 10^{46} \text{ erg s}^{-1}$.

(v) A nuclear ionized outflow driven by the nuclear activity was identified in the SDSS optical spectrum of this QSO (VM14), with FWHM $\sim 970 \text{ km s}^{-1}$ and a velocity blueshift $V_s \sim -90 \text{ km s}^{-1}$.

2 OBSERVATIONS, DATA REDUCTION AND ANALYSIS

2.1 GTC imaging

2.1.1 Observations

H α Tunable Filter (TF) imaging observations were taken in service mode on 2014 July 25 (programme GTC37-14A) for the ‘Beetle’ using the optical images and long-slit spectrograph OSIRIS⁴ mounted on the 10.4-m GTC. OSIRIS consists of a mosaic of two 2048×4096 Marconi CCD42-82 (with a 9.4 arcsec gap between them) and covers the wavelength range from 0.365 to 1.05 μm with a field of view of 7.8 arcmin \times 7.8 arcmin and a pixel size of 0.127 arcsec. However, the OSIRIS standard observation modes use 2×2 binning, hence the effective pixel size during our observations was 0.254 arcsec.

Our goal is to detect extended ionized gas (H α) associated with the QSO2. For this, a filter FWHM of 20 \AA was used ($\sim 830 \text{ km s}^{-1}$ at the QSO2 z) centred on the redshifted H α and taking into account the dependence of the wavelength observed with the red TF with distance relative to the optical centre. The order sorter filter *f723/45* was also used. The FWHM is adequate to cover the velocity range expected to be spanned by any plausible extended ionized features. Contamination by [N II] $\lambda\lambda 6548, 6583$ is expected to be negligible, since the lines are located at -16.5 \AA and $+22 \text{ \AA}$ relative to H α , and H α is the strongest of the three lines at all locations (our long spectroscopy confirms this). The total exposure time on source was 2700 s distributed in 3×900 s exposures. To be able to correct for ghost images and cosmic rays, we dithered between three positions, moving the telescope ± 15 arcsec in RA and Dec.

To sample the continuum near the H α +[N II] complex, we took one continuum image to the blue of H α using directly the OSIRIS Red Order Sorter (OS) Filter *f666/36*, which covers the 6490–6845 \AA spectral window (5884–6206 \AA rest frame). This filter was used to avoid emission line contamination (by, for instance, [O I] $\lambda 6300$). The disadvantage is that objects with a steep continuum slope (for instance, very red objects) will leave prominent residuals due to the significant shift in λ relative to H α . Thanks to the complementary spectroscopic data, we can confirm that this has no impact on our analysis and interpretation. The total exposure time of the continuum image was 600 s split into 3×200 s exposure. The same dithering pattern was applied as for the H α image.

2.1.2 Reduction process

The TF and the OS filter OSIRIS images were bias and flat-field corrected as usual, using a set of bias frames and dome flats.

We observed a photometric standard star for flux calibration using the exact same set-up as the one used for the science object. After correcting the corresponding frames for bias and flat-field, we applied aperture photometry using the routine `PHOT` in `PYRAF`. The `PHOT` output gives us the integrated number of counts within the aperture

for the standard star observed. We then used a customized `PYTHON` routine that generates a TF transmission curve for a given central wavelength and FWHM. The resulting TF transmission curve was normalized and multiplied by the spectra of the standard star in units of $\text{erg s}^{-1} \text{ cm}^{-2} \text{ \AA}^{-1}$. This gives us the expected flux of the standard star in the corresponding TF and OS filter in units of $\text{erg s}^{-1} \text{ cm}^{-2}$. We then multiply these numbers by the exposure time used for the standard star observations and divide the result by the output from `PHOT`. The result will be a flux calibration factor (F) in units of $\text{erg cm}^{-2} \text{ counts}^{-1}$. Finally, to calibrate in flux our science frames we divide them by their corresponding exposure times and multiply them by F , which transforms the units of the frames after bias and flat-field correction (counts) into $\text{erg s}^{-1} \text{ cm}^{-2}$.

Once the images are calibrated in flux, we need to subtract the sky emission. When using a TF imaging technique, the wavelength observed changes relative to the optical centre. In the case of OSIRIS, this change is given by González et al. (2014):

$$\lambda = \lambda_0 - 5.04 * r^2, \quad (1)$$

where λ_0 is the wavelength in \AA at the optical centre, located at pixel (2098, 1952) of CCD1 in the case of OSIRIS, and r is the distance from that centre in arcmin. Therefore, the different sky lines around the wavelength range selected for the observations are observed in the form of rings of emission spread over the CCDs. This effect becomes important if the sample objects are relatively extended and a careful sky emission subtraction must be performed.

With this aim, we first cut a rectangular region of the CCD that is large enough to contain a sizeable region of the sky, and small enough so that the effects of the sky emission rings are reduced to the minimum possible. Then, we used `FIT1D` in `PYRAF` to fit a 1D polynomial function to the overall structure in the x and y direction, respectively. The first x/y 1D fit is performed only on sky regions free from emission from stars in the frame and the target observation, and it is then extended through the entire rectangular cut. The following y/x is applied to all the rectangular cut at once. The result of this process is a synthetic image containing only the sky emission. Then, this image is directly subtracted from the original flux-calibrated image of the source resulting in an image cleaned from any background and sky emission.

The next step during the reduction process is subtracting the continuum from the emission line image. Prior to this, they were geometrically aligned. Based on the centroid of the stars in the aligned images and the position of some important features in the galaxy, we estimate that the alignment accuracy is better than 0.5 pixels. The continuum emission was then subtracted from the emission line image in order to produce the final ‘pure’ H α image.

2.2 GTC long-slit spectroscopy

Long-slit spectroscopic observations were performed in service mode with OSIRIS on GTC between 2015 June 26 and July 23 (programme GTC1-15A). The *R2500V* and *R2500R* volume-phased holographic gratings (VPHs) were used, that provide a spectral coverage of 4500–6000 \AA and 5575–7685 \AA , respectively, with dispersions of 0.8 and 1.04 \AA pixel^{-1} . A 1.23 arcsec slit width was used at three different orientations (position angle PA 0° , PA 48° and PA 83°)⁵ in order to map the emission around the quasar. The spectral resolution $\text{FWHM}_{\text{inst}}$ measured from several prominent sky lines is

⁴ <http://www.gtc.iac.es/en/pages/instrumentation/osiris.php>

⁵ All position angles throughout the text are quoted N to E.

Table 1. Log of the GTC Osiris long-slit spectroscopic observations.

Obs. date	PA (°) (N to E)	Exposure <i>R2500V</i>	Exposure <i>R2500R</i>	Airmass	Seeing
26–27/06/2015	48	18 × 300 s	–	1.4	0.9 arcsec
17/07/2015	48	–	16 × 300 s	1.2	0.9 arcsec
18/07/2015	0	8 × 300 s	8 × 300 s	1.1	1.1 arcsec
23/07/2015	83	8 × 300 s	4 × 300 s	1.1	1.2 arcsec
07/03/2016	140	3 × 900 s	–	1.1	1.0 arcsec

3.37 ± 0.13 and $4.41 \pm 0.06 \text{ \AA}$ for *R2500V* and *R2500R*, respectively. Several 300 second spectra were obtained at each orientation (Table 1), with shifts in the slit direction of 20 arcsec between consecutive exposures for both a better fringing correction and a more accurate background subtraction.

Additionally, a series of $3 \times 900 \text{ s}$ *R2500V* spectra were taken on 07/03/2016 under GTC Directors Discretionary Time (programme GTC01-16ADDT). The same slit width was used with PA 140° . Those spectra were obtained avoiding the quasar nucleus and roughly perpendicular to the main radio axis (PA 48°).

2.2.1 Reduction process and spectral fitting

The reduction of the spectra was done using standard procedures and IRAF tasks. Images were first bias and flat-field corrected, by using lamp flats. The 2D spectra were wavelength calibrated using Xe+Ne+HgAr lamps, with a resulting error consistent with the nominal spectral resolutions of the VPHs. After the wavelength calibration, sky background was subtracted and a 2D spectrum was obtained. Flux calibration was done using observations of spectrophotometric standard stars, white dwarfs, obtained the same nights as the scientific spectra. Finally, the different individual spectra were averaged, obtaining a mean spectrum for each of the orientations.

Like the images, the spectra were corrected for atmospheric and foreground galactic extinction ($A_V = 0.153$).

The spectral profiles of the nuclear emission lines are complex (several kinematic components). They were fitted following the multi-Gaussian procedure described in detail in Villar Martín et al. (2016). In order to have a more realistic estimation of the uncertainties, whenever possible, the lines were fitted in two different ways: (a) with kinematic constraints based on the results of the $[\text{O III}] \lambda\lambda 4949, 5007$ fits and (b) without prior kinematic constraints. When both methods provided fits of similar quality, the fitted parameter values (fluxes, FWHM and V_c) are the average of all fits. The error for each parameter is chosen as the largest value between the fit errors and the standard deviation of all valid fits (see Villar Martín et al. 2016 for more details). The FWHM values were corrected for instrumental broadening by subtracting the instrumental profile $\text{FWHM}_{\text{inst}}$ in quadrature.

When physically meaningful or mathematically valid fits (e.g. for faint emission lines) could not be obtained without kinematic constraints, the $[\text{O III}]$ doublet lines were used as reference to force the individual kinematic components to have the same velocity shift and/or FWHM.

2.3 VLA radio maps

Observations with the Karl G. Jansky VLA were performed on 2015 July 13 and 18 with the A-configuration (programme 15A-237) and on 2016 June 1 with the B-configuration (programme 16A-088).

The on-source exposure time in A-configuration was 0.7 h and in the B-configuration 3 h.

The correlator was set to produce a 1 GHz bandwidth, ranging from 1 to 2 GHz, with 1 MHz channels. We used 3C 286 for flux calibration, and obtained a 5 min scan on the strong ($\sim 5 \text{ Jy}$) source J1609+2641 every ~ 50 min for both phase and bandpass calibration. Flagging of radio-frequency interference, which affected ~ 40 per cent of our data, as well as a standard bandpass, phase and flux calibration was performed using the VLA data reduction pipeline in the Common Astronomy Software Applications (CASA) v. 4.6 (McMullin et al. 2007). We manually inspected the pipeline-calibrated data to ensure that the quality of the data products was sufficient for further reduction. We subsequently applied one self-calibration to the A-configuration data and two iterative self-calibrations to the B-configuration data to improve the phases.

The data were imaged by applying a Fourier transform using a multifrequency synthesis technique, and subsequently cleaning the continuum signal. We imaged the A-configuration data using uniform weighting, which resulted in a beam of 0.80×0.74 arcsec (PA = $41^\circ:8$) and rms noise level of $0.066 \text{ mJy beam}^{-1}$. We also imaged the A-configuration data using robust +0.3 weighting (Briggs 1995), which resulted in a beam of 1.05×0.97 (PA = $47^\circ:7$) arcsec and rms noise level of $0.018 \text{ mJy beam}^{-1}$. The B-configuration data were imaged using robust +0.3 weighting (Briggs 1995), which resulted in a beam of $3.52 \text{ arcsec} \times 3.25 \text{ arcsec}$ (PA = $53^\circ:8$) and rms noise level of $0.013 \text{ mJy beam}^{-1}$.

The B-configuration data revealed the radio continuum from star formation in two galaxies, the companion galaxy ~ 11 arcsec or ~ 20 kpc south of the ‘Beetle’ and a galaxy ~ 42 arcsec or ~ 78 kpc NE. This allowed us to overlay the radio and optical images to within an estimated accuracy of ~ 0.6 arcsec.

3 ANALYSIS AND RESULTS

3.1 Radio versus optical morphology

The continuum image of the ‘Beetle’ (Fig. 2, left) reveals an elliptical galaxy with clear signatures of a merger/interaction event, such as shells and filaments. The shells do not completely encircle the central galaxy and their main axis is aligned with the galaxy major axis. This has been observed in other elliptical galaxies with high ellipticity (e.g. Athanassoula & Bosma 1985; Duc et al. 2015) as is the case for the ‘Beetle’ ($e = b/a = 0.78$, Vizier catalogue based on Hakobyan et al. 2009). Simulations of galactic interactions show that such shells may result from (nearly) head-on collisions with smaller disc galaxies (e.g. Quinn 1984; Struck 1999). The interacting galaxy is probably the smaller galaxy

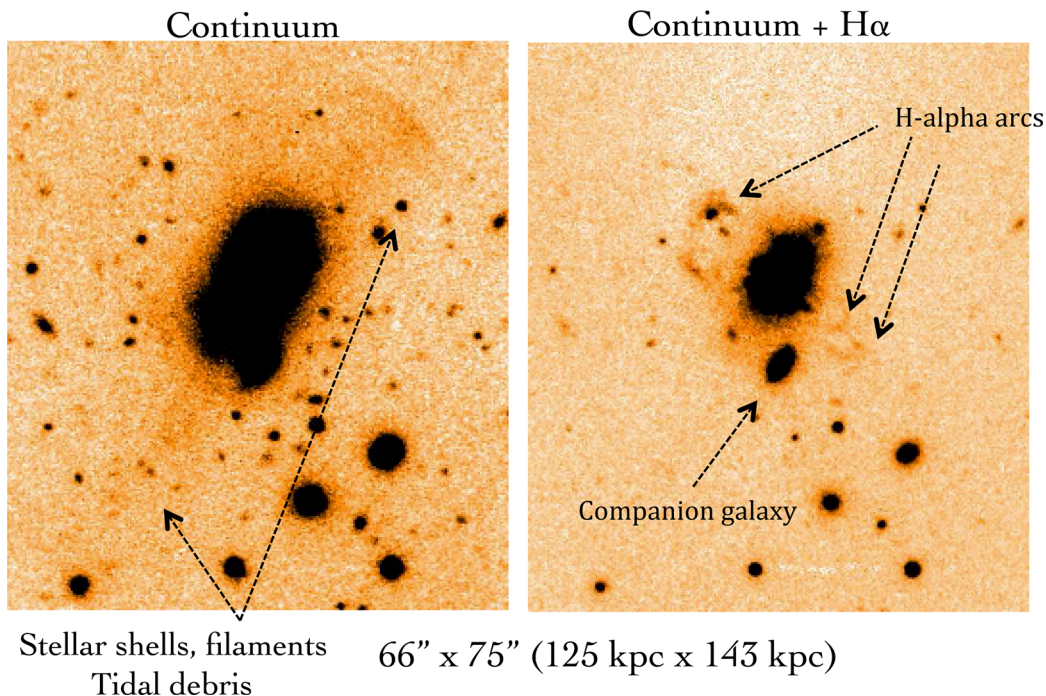


Figure 2. Left: optical GTC-Osiris continuum (left) and narrow band $H\alpha$ +continuum (right) images of the ‘Beetle’. Both images show the same field of view. The continuum image shows prominent tidal features (shells, filaments) well outside the main body of the galaxy. They are not detected in the narrow band image. This shows instead an intricate set of knots/arcs, shaping structures reminiscent of optical bubbles or bow shocks. They run roughly perpendicular to the main galaxy axis and the axis of the tidal debris identified in the continuum image. The filaments are not detected in the continuum image. They consist of ionized gas.

located ~ 11 arcsec or ~ 20 kpc south of the QSO⁶ (Fig. 2). The GTC-OSIRIS optical spectra of this object show that it is at the same $z = 0.10351 \pm 0.00008$ as the ‘Beetle’ (Fig. 3). Based on the $[O\text{III}]/H\beta = 0.70 \pm 0.05$, $[N\text{II}]/H\alpha = 0.34 \pm 0.03$, $[S\text{II}]/H\alpha = 0.46 \pm 0.03$ and $[O\text{I}]/H\alpha = 0.06 \pm 0.01$ ratios, it is classified as a star-forming galaxy (Baldwin, Philips & Tevich 1981; Kewley et al. 2006).

The $H\alpha$ +continuum narrow band image reveals a spectacular structure of knots and arcs (Fig. 2, right), with a main axis that runs perpendicular to the main galaxy axis and the complex stellar tidal debris seen in the continuum image. Three arcs are identified, which are not detected in the continuum image. This already suggests that they are emission line dominated features, as confirmed by the continuum subtracted $H\alpha$ image (Fig. 4). One arc is located at ~ 13.5 arcsec (25 kpc) to the NE from the QSO2 centroid. Two more are at ~ 10.2 arcsec (19 kpc) and ~ 13.7 arcsec (26 kpc) SW of the QSO2. Thus, these features are in the circumgalactic environment.

The morphology of the arcs is reminiscent of optical bow shocks seen in some powerful radio galaxies, where the extended radio structures are interacting with the environment (e.g. Coma A, Tadhunter et al. 2000; see also Harrison et al. 2015 for a related example of a radio-quiet QSO2: the ‘Teacup’). The ‘Beetle’ is certainly not associated with such a luminous radio source as Coma A (it is ~ 300 times fainter) and is classified as radio quiet. However, based on this resemblance a scenario of radio jets/lobes being responsible for the observed optical ionized gas features appears plausible. This prompted us to obtain a deeper radio map that has

confirmed the existence of a previously unknown extended radio source.

The VLA observations reveal a radio source with a total extent of ~ 24.5 arcsec or ~ 46 kpc (Fig. 4). We detected two outer hotspots at ~ 14 arcsec NE and ~ 10.5 arcsec SW from the radio core, respectively. Therefore, the two hotspots overlap with the NE and inner SW arcs.

Fig. 4 (middle panel) shows our VLA high-resolution (A-configuration) radio map of the Beetle. The inner radio jet is detected across a total extent of ~ 2.3 arcsec or ~ 4.3 kpc (right-hand panel). It consists of a bright hotspot ~ 0.8 arcsec or ~ 1.5 kpc towards the SW and fainter emission towards the NE. If this is a result of Doppler boosting, it suggests that the inner jet is approaching on the SW side and receding on the NE side. This is consistent with the outer lobe shown in the low-resolution map (B-configuration, Fig. 4, left). Only on the SW side, we detect an outer radio lobe that connects the inner radio emission to the outer SW hotspot. This indicates that the SW side of the radio source is Doppler boosted and approaching also on large scales. Interestingly, while the modest radio power of the ‘Beetle’ is typical of FR-I sources, the hotspot morphology resembles more closely that of the Fanaroff–Riley type-II (FR-II) sources (Fanaroff & Riley 1974).

Our current data do not reveal whether the radio core represents re-started activity, or forms a continuous structure with the outer radio lobes and hotspots. However, the inner jet has PA 68° . If we extrapolate its axis towards the NE, it seems to cross the northern $H\alpha$ arc at a location where this appears broken. This may suggest that the radio core is actively feeding the outer lobes. The angle between the inner jet and the outer radio axis is 19° , which would indicate precession of the radio jet or bending as it propagates outward. A deeper radio map might reveal a fainter, so far unseen extended radio structure that may have perforated the northern arc.

⁶ All quoted distances and sizes will be projected values unless otherwise specified.

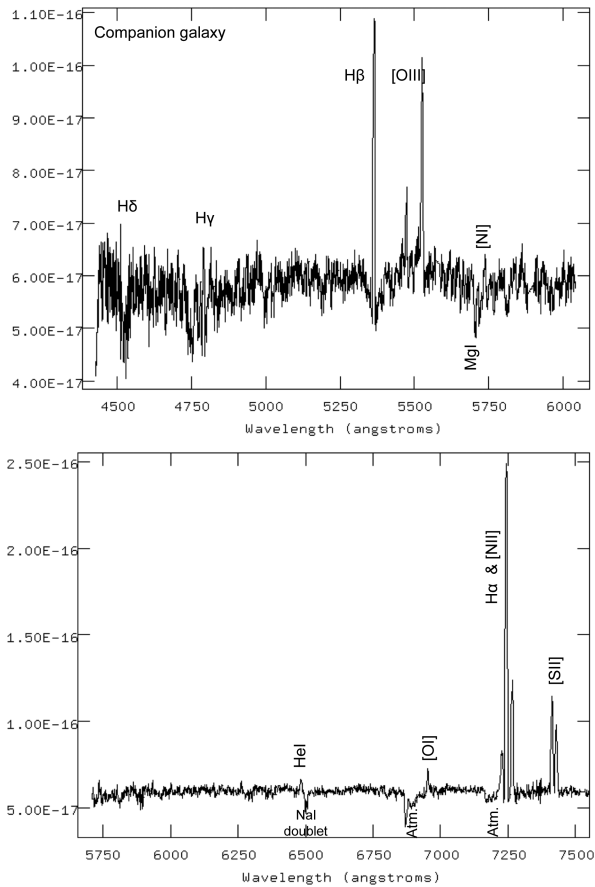


Figure 3. Spectra (observed frame) of the star-forming companion galaxy. Prominent emission and absorption features are identified. ‘Atm.’ marks atmospheric absorption bands. The flux is in $\text{erg s}^{-1} \text{cm}^{-2} \text{\AA}^{-1}$.

The radio and emission line morphologies are closely correlated. The large-scale radio axis is the same as the axis defined by the brightest $\text{H}\alpha$ knots. In fact, the NE radio hotspot overlaps with the brightest circumgalactic $\text{H}\alpha$ feature. The centre of the southern

arc closer to the galaxy overlaps with the SW radio hotspot. The close correlation between the radio and $\text{H}\alpha$ morphologies suggests that the interaction of the radio structures with the CGM shapes the morphology of the large-scale ionized gas, possibly also of the radio source (alternative, less convincing scenarios will be discussed in Section 4).

While the NE radio hotspot seems to define roughly the edge of the NE ionized structures, the optical line emission extends well beyond the SW radio hotspot. This will be further discussed below based on the spectroscopic data.

3.2 The nuclear outflow

3.2.1 Physical properties and excitation mechanism

The results of the fits of the nuclear emission lines are shown in Table 2 and Fig. 5. Three kinematic components are isolated in the $[\text{O III}] \lambda\lambda 4959, 5007$ lines with $\text{FWHM} = 144 \pm 3, 398 \pm 36$ and $973 \pm 25 \text{ km s}^{-1}$, respectively. The broadest component traces the ionized outflow. It is blueshifted by $-144 \pm 6 \text{ km s}^{-1}$, relative to the narrowest component. These values are in agreement with those obtained by VM14 based on the SDSS optical spectrum. The fits to the rest of the main optical lines produce consistent results within the errors. As already pointed out by VM14, the line ratios place the three kinematic components, including the outflow, in the AGN area of the diagnostic diagrams (Baldwin et al. 1981; Kewley et al. 2006).

The reddening $E(B - V)$, electron density n_e and temperature T_e have been inferred for the three kinematic components using $\text{H}\alpha/\text{H}\beta$ ($\text{H}\gamma/\text{H}\beta$ is affected by large uncertainties especially for the outflowing gas; see Fig. 5), $[\text{S II}] \lambda 6716/\lambda 6731$ and reddening corrected $[\text{O III}] \lambda\lambda 4959, 5007/\lambda 4363$, respectively (Table 3).

Inferring n_e for the outflow is not trivial, given the complexity of the $[\text{S II}]$ doublet (three components per line) and the partial blend of both lines (Fig. 6). It is found that the fits producing kinematically reasonable results (in comparison with the other emission lines) and physically meaningful results (as opposite to unphysical, such as $[\text{S II}] \lambda 6716/\lambda 6731 > 1.4$ for any of the individual components) result in $[\text{S II}] \lambda 6716/\lambda 6731 = 0.69 \pm 0.20$, as indicated

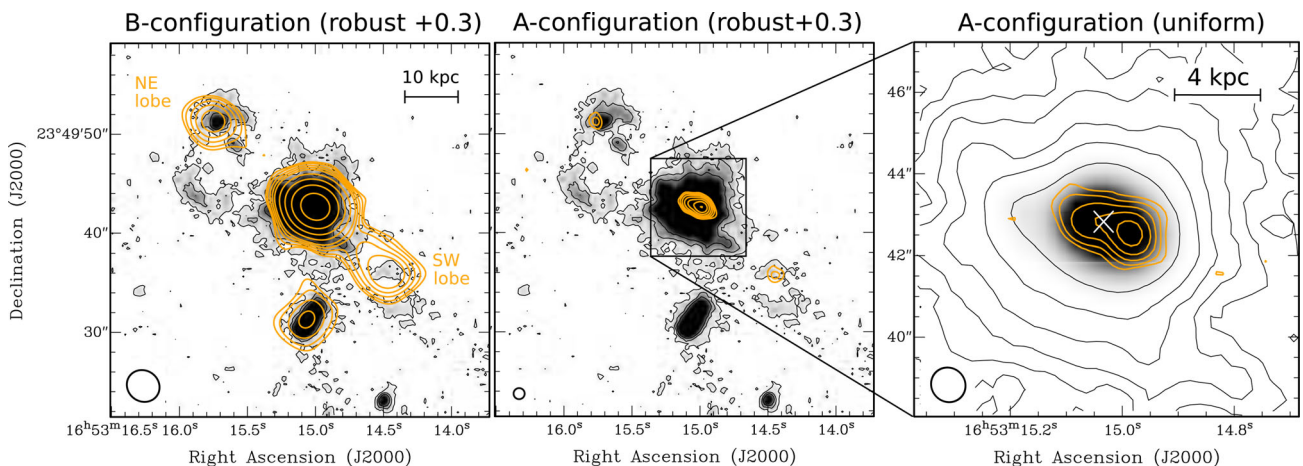


Figure 4. GTC $\text{H}\alpha$ (continuum subtracted) image (grey) and VLA 1.4 GHz continuum contours (orange) of the ‘Beetle’. Left: VLA B-configuration data with robust +0.3 weighting. Contour levels: 0.063, 0.085, 0.13, 0.18, 0.25, 0.50, 1.0, 2.0, 4.0 mJy beam^{-1} . Middle: VLA A-configuration data with robust +0.3 weighting. Contour levels: 0.08, 0.16, 0.32, 0.64, 1.3, 2.5, 5.0 mJy beam^{-1} . The outer radio hotspots overlap with the head of the $\text{H}\alpha$ arcs, suggesting that the interaction between the radio structures and the ambient gas is responsible for the morphology of the large-scale circumgalactic ionized gas. Right: zoom-in of the core region, showing the VLA A-configuration data with uniform weighting. Contour levels: 0.2, 0.4, 0.8, 1.6, 3.2 mJy beam^{-1} . The beam of the various VLA data sets is shown in the bottom left of each plot.

Table 2. Results of the nuclear fits. The properties of the individual kinematic components are shown. The velocity shifts V_s have been calculated relative to the λ of the narrowest component. Numbers in italics correspond to lines for which the kinematic parameters have been fully constrained with other emission lines (hence no errors).

Narrow component	FWHM (km s ⁻¹)	V_s (km s ⁻¹)	Flux $\times 10^{-15}$ (erg s ⁻¹)
[O III] λ 5007	144 \pm 3	0 \pm 3	49.8 \pm 0.7
H β	127 \pm 25	0 \pm 3	2.2 \pm 0.4
H γ	<i>144</i>	0 \pm 3	1.2 \pm 0.1
[O III] λ 4363	<i>144</i>	0 \pm 3	0.8 \pm 0.1
H α	113 \pm 11	0 \pm 3	5.6 \pm 0.3
[N II] λ 6583	<i>113 \pm 11</i>	0 \pm 3	2.3 \pm 0.1
[S II] λ 6716	91 \pm 18	0 \pm 4	0.6 \pm 0.1
[S II] λ 6731	<i>91</i>	0	0.6 \pm 0.1
Intermediate component	FWHM	V_s	Flux
[O III] λ 5007	398 \pm 36	-105 \pm 3	74.5 \pm 0.3
H β	398 \pm 13	-105 \pm 5	9.2 \pm 0.3
H γ	398	-91 \pm 10	3.2 \pm 0.2
[O III] λ 4363	398	-91 \pm 10	1.3 \pm 0.2
H α	387 \pm 3	-126 \pm 3	37.5 \pm 0.5
[N II] λ 6583	<i>387 \pm 3</i>	<i>-126 \pm 3</i>	13.0 \pm 0.3
[S II] λ 6716	392 \pm 4	-119 \pm 3	7.7 \pm 0.2
[S II] λ 6731	<i>392</i>	<i>-119</i>	6.9 \pm 0.2
Broad component	FWHM	V_s	Flux
[O III] λ 5007	973 \pm 25	-144 \pm 6	22.9 \pm 0.9
H β	942 \pm 78	-195 \pm 84	1.3 \pm 0.2
H γ	973	-128 \pm 16	1.1 \pm 0.3
[O III] λ 4363	973	-128 \pm 16	0.7 \pm 0.2
H α	1267 \pm 174	-235 \pm 40	7.4 \pm 0.8
[N II] λ 6583	<i>1267 \pm 174</i>	<i>-235 \pm 40</i>	3.0 \pm 0.7
[S II] λ 6716	1000 \pm 75	-320 \pm 56	0.9 \pm 0.2
[S II] λ 6731	<i>1000</i>	<i>-320</i>	1.3 \pm 0.3

in Table 3. This implies $n_e = 2571^{+14181}_{-1461} \text{ cm}^{-3}$ for the outflowing gas. The minimum possible value of the [S II] ratio (0.49) is actually in the regime where the ratio saturates and becomes insensitive to increasing densities (Osterbrock 1989). Thus, the ‘best’ density $n_e = 2571 \text{ cm}^{-3}$ is effectively almost a lower limit. The outflowing gas density is substantially higher than the densities of the narrow ($n_e = 730^{+634}_{-365} \text{ cm}^{-3}$) and the intermediate ($n_e = 425^{+89}_{-78} \text{ cm}^{-3}$) components, respectively. Different works suggest that such high densities are frequent in the nuclear ionized outflows of luminous type 2 AGNs (e.g. Holt et al. 2011; VM14; Villar Martín et al. 2015).

We have tested whether a good fit can also be obtained by forcing the broadest component to have low density ([S II] λ 6716/ λ 6731 = 1.4 or $n_e \lesssim 100 \text{ cm}^{-3}$; Osterbrock 1989). However, we get reasonable fits only under very strict constraints on the kinematics and individual line ratios. We thus consider that the higher densities are more realistic. This is supported also by the high [O III]/H β = 17.8 \pm 3.3 ratio, which points to $n_e \sim \text{few} \times 1000\text{--}10^4 \text{ cm}^{-3}$ (VM14). High densities in the narrow-line region of the ‘Beetle’, where the gas emitting the broadest component is likely to be located, are also suggested by [Ar IV] λ 4711/ λ 4740 = 1.10 \pm 0.08, which implies $n_e = 3450^{+1280}_{-1127}$, i.e. at least $n_e \sim 2300 \text{ cm}^{-3}$.

The nuclear outflow shows the highest reddening of the three kinematic components with H α /H β = 5.8 \pm 1.2, as often found for the ionized outflows in QSO2 (VM14). As proposed by Villar Martín et al. (2015), the trend of the outflowing gas to have the

highest reddening and density can be naturally explained if the outflow is concentrated in a smaller region, closer to the AGN than the intermediate and narrow components (Bennert et al. 2006a,b). It also shows significantly higher $T_{e4} = \frac{T_e}{10^4} = 2.2^{+4.6}_{-0.5} \text{ K}$, compared with 1.38 $^{+0.08}_{-0.07}$ and 1.56 $^{+0.19}_{-0.13} \text{ K}$ for the narrow and intermediate components, respectively. The additional heating may be produced by shocks induced by the outflow (e.g. Villar Martín et al. 1999).

3.2.2 Radial size

We have derived the radial size R_o of the nuclear outflow along the three different slit PAs. Upper limits or actual sizes are constrained by comparing the spatial distribution of the broadest kinematic component and the seeing profile. Lower limits are obtained by applying the spectroastrometric method (see Carniani et al. 2015 and Villar Martín et al. 2016 for a detailed description and discussion on the uncertainties of both methods).

The method of spectroastrometry, which gives lower limits, consists of measuring the relative position of the centroid of the [O III] spatial profile as a function of velocity. We assume as spatial zero the continuum centroid. Although this does not necessarily mark the exact location of the AGN, it is a reasonable assumption for our purposes, since the associated uncertainty on R_o is expected to be $\lesssim \text{few} \times 100 \text{ pc}$. We consider as zero velocity that of the narrow core of the [O III] nuclear line. The results are shown in Fig. 7. We infer $R_o \gtrsim 1.2 \text{ kpc}$, $\gtrsim 1.3 \text{ kpc}$ and $\gtrsim 0.5 \text{ kpc}$ along PA48, PA83 and PA0, respectively.

To compare the seeing profile with the spatial distribution of the outflow, a spatial profile of the [O III] line (continuum subtracted) was extracted from a spectral (velocity) window clearly dominated by the outflow. As discussed in Villar Martín et al. (2016), it is essential to use an accurate seeing profile for a reliable assessment of any possible excess above the seeing distribution, especially the wings. Following that work, the seeing profiles along PA48, PA83 and PA0 were specifically built using non-saturated stars with well-detected wings in the acquisition images obtained at similar time as the spectra. The seeing profiles were extracted from apertures of the same width in arcsec as the narrow slit of the spectroscopic observations.

The outflow spatial distribution is found to be resolved (FWHM_{obs} = 1.25 \pm 0.05 arcsec) relative to the seeing (FWHM = 0.85 \pm 0.04 arcsec) only along PA48 (Fig. 8). We obtain $R_o = 0.86 \pm 0.07 \text{ kpc}$ after correcting for seeing broadening. The error accounts for the uncertainty on FWHM_{obs} and the seeing FWHM. All uncertainties considered, this R_o is in good agreement with the spectroastrometric result ($R_o \gtrsim 1.2 \text{ kpc}$).

The same method demonstrates that the outflow spatial distribution is consistent with the seeing disc along both PA83 (seeing FWHM = 1.25 \pm 0.07 arcsec) and PA0 (seeing FWHM = 1.1 \pm 0.1 arcsec). This implies $R_o \lesssim 0.7$ and 0.8 kpc, respectively, also in reasonable agreement with the spectroastrometric lower limits taking into account all uncertainties.

3.2.3 Mass and energetics

Following standard procedures (see Villar Martín et al. 2016 for a discussion on the method and all related uncertainties), we have calculated the outflow mass M_o , mass outflow rate \dot{M}_o , energy \dot{E}_o and momentum \dot{p}_o injection rates. We assume $n_e = 2571 \text{ cm}^{-3}$, $V_o = |V_s| + \text{FWHM}/2 = 630 \text{ km s}^{-1}$ (see Tables 2 and 3; Arribas et al. 2014) and $R_o = 0.86 \text{ kpc}$. The H β flux of the outflowing component isolated in the nuclear spectrum is

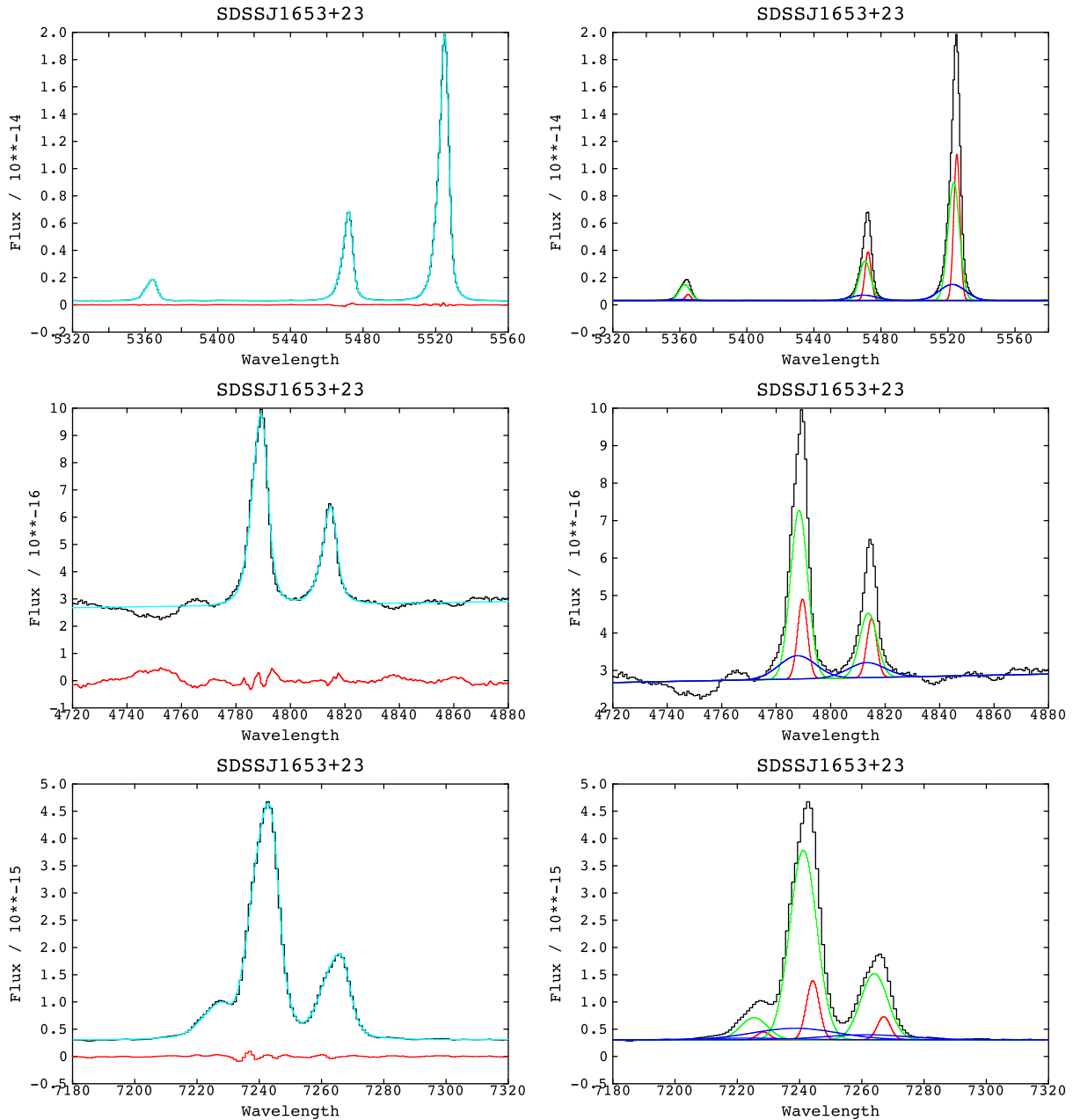


Figure 5. Fits of the main nuclear emission lines. From top to bottom: [O III] and H β , H γ and [O III] λ 4363, H α and [N II] $\lambda\lambda$ 6548,6583. The data, the fits and residuals are shown in black, cyan and red, respectively (left-hand panels). The individual components are shown in the right-hand panels with different colours. Red (narrow component), green (intermediate) and blue (broad) are used from the most redshifted to the more blueshifted components.

$F(\text{H } \beta_o) = (1.3 \pm 0.2) \times 10^{-15} \text{ erg s}^{-1}$. Slit losses are expected to be small [$F(\text{H } \beta_o) = (1.5 \pm 0.2) \times 10^{-15} \text{ erg s}^{-1}$] as measured from the SDSS 3 arcsec fibre spectrum, VM14]. Correcting for reddening (as implied by H α /H $\beta \sim 5.8$), the outflow luminosity is $L(\text{H } \beta_o) \sim 3.2 \times 10^{41} \text{ erg s}^{-1}$. Therefore, $\dot{M}_o = 3.5 \times 10^6 M_\odot$ and $\dot{M}_o = 2.6 M_\odot \text{ yr}^{-1}$. In addition, $\dot{E}_o = 3.2 \times 10^{41} \text{ erg s}^{-1}$ (or $\sim 10^{-5} \times L_{\text{Edd}}$) and $\dot{p}_o = 1.0 \times 10^{34} \text{ dyne}$ (or $\sim 0.01 L_{\text{Edd}}/c$), where L_{Edd} is the Eddington luminosity (Section 1.1).

As discussed in Villar Martín et al. (2016), the outflowing gas is likely to have a density gradient with increasing densities at decreasing distances from the AGN. If such is the case, the assumption of higher densities would result in even lower values.

3.3 The circumgalactic gas

We have studied the spatial distribution and properties of the ionized gas along the four slit PAs described in Section 2.2. 1D spectra were extracted from different apertures centred on prominent emission line features detected along each slit and low surface brightness regions in between. The slit locations, the 2D spectra of the [O III] doublet and the apertures used for our study are shown in Figs 9 and 10.

3.3.1 Spatial extension of the emission lines

Extended ionized gas is detected along the four slit PAs (Table 4). The maximum extension is measured along PA48 (i.e. the

Table 3. Line ratios (not corrected for reddening) and physical properties of the nuclear total spectrum and the individual kinematic components. The electron temperature T_e has been calculated using the reddening corrected $[\text{O III}]\lambda 4959, 5007/[\text{O III}]\lambda 4363$ ratio.

Ratio	Narrow	Intermediate	Broad	Total
$[\text{O III}]\lambda 5007/\text{H } \beta$	22.2 ± 4.3	8.1 ± 0.3	17.8 ± 3.3	11.9 ± 0.3
$\text{H } \gamma/\text{H } \beta$	0.54 ± 0.12	0.35 ± 0.03	0.84 ± 0.30	0.43 ± 0.08
$[\text{O III}]\lambda 4959, 5007/[\text{O III}]\lambda 4363$	84 ± 11	76 ± 12	54 ± 11	73 ± 7
$\text{H } \alpha/\text{H } \beta$	2.6 ± 0.5	4.1 ± 0.2	5.8 ± 1.2	3.98 ± 0.07
$[\text{N II}]\lambda 6583/\text{H } \alpha$	0.41 ± 0.04	0.35 ± 0.01	0.40 ± 0.10	0.36 ± 0.02
$[\text{S II}]\lambda 6716, 6731/\text{H } \alpha$	0.22 ± 0.02	0.39 ± 0.01	0.29 ± 0.05	0.36 ± 0.01
$[\text{S II}]\lambda 6716/[\text{S II}]\lambda 6731$	0.99 ± 0.15	1.11 ± 0.04	0.69 ± 0.20	1.04 ± 0.05
n_e (cm^{-3})	730_{-365}^{+634}	425_{-78}^{+89}	2571_{-1461}^{+14181}	588_{-223}^{+111}
$E(B - V)$	0	0.33 ± 0.04	0.63 ± 0.18	0.30 ± 0.02
T_e ($\times 10^4$ K)	$1.38_{-0.07}^{+0.08}$	$1.56_{-0.13}^{+0.19}$	$2.2_{-0.5}^{+4.6}$	$1.62_{-0.08}^{+0.10}$

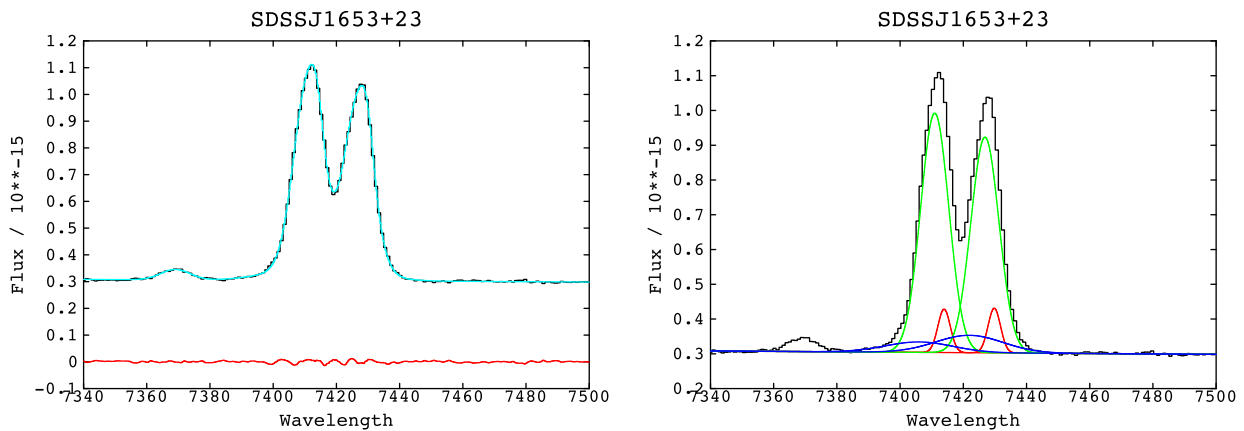


Figure 6. Fit of the $[\text{S II}]\lambda\lambda 6716, 6731$ doublet. The broadest component has high density with $[\text{S II}]\lambda 6716/\lambda 6731 = 0.69 \pm 0.20$. The error includes the uncertainty due to the range of acceptable fits. Colour code as in Fig. 5.

radio hotspots axis, Fig. 9), with line emission detected across $D_{\text{max}} \sim 38$ arcsec or 71 kpc. Towards the NE, as already seen in the $\text{H } \alpha$ image, the brightest $[\text{O III}]$ emission overlaps with the NE hotspot. Towards the SW, line emission is detected well beyond the hotspot. A compact (along the slit) emission line feature is detected at ~ 10.5 arcsec or ~ 20 kpc beyond the hotspot and $R_{\text{max}} \sim 41$ kpc from the QSO2 centroid [aperture (ap.) G in Fig. 9]. Line emission is detected also between the high surface brightness features, at least from ap. A to F.

Along PA83 the spatial distribution of the emission lines is highly asymmetric. $D_{\text{max}} \sim R_{\text{max}} \sim 23$ kpc towards the E, up to the eastern edge of the $\text{H } \alpha$ bubble identified in the narrow band image (ap. H, Fig. 10). Towards the W, the lines are just barely resolved compared with the seeing disc.

Along PA0, extended line emission associated with the QSO2 is tentatively detected only towards the N, up to $R_{\text{max}} \sim 29$ kpc. This detection is confirmed by the PA140 spectrum (Fig. 10). Along this PA, which did not cross the galactic nucleus, the line emission extends at both sides of the radio axis across $D_{\text{max}} \sim 23$ arcsec or 43 kpc. This suggests that line emission is detected across the entire area delineated by the NW edge-brightened bubble.

3.3.2 Kinematics

The visual inspection of the 2D $[\text{O III}]$ spectra reveals variations on the kinematic properties of the gas (FWHM and V_s) correlated

with the radio structures. This is particularly striking along the radio axis (PA48) and PA140. Along PA48 (Fig. 9), the lines are clearly broader at the location of the NE hotspot. Moreover, a broad blueshifted wing is detected at the location of the SW hotspot. A sharp, continuous change in V_s of ~ 550 km s^{-1} occurs in aperture C (Fig. 9, right-hand panel) in a region of very low surface brightness. Along PA140, the lines appear clearly split in two components at the location crossing the radio axis (see aperture K in Fig. 10, bottom right panel).

We show in Fig. 11 (left-hand panels) how the kinematics of the ionized gas varies spatially along PA48. The lines were fitted with 1 or 2 Gaussians, as required, using the 1D spectra extracted from each aperture (Fig. 9). FWHM and V_s are plotted at each location for the individual kinematic components. The three components identified in the nuclear spectrum (see Section 3.2) are also plotted at the spatial zero. The variation of the $[\text{O III}]/\text{H } \beta$ ratio is shown when measurable.

Two kinematic components are required to fit $[\text{O III}]$ across the spatial range circumscribed by the radio hotspots (a single component is required beyond). The narrowest component has an $\text{FWHM} \lesssim 150$ km s^{-1} and extends all the way along the slit, including beyond the maximum observed spatial extent of the radio emission. In contrast, a broader component of $\text{FWHM} \sim 380$ – 470 km s^{-1} is detected across the entire spatial range circumscribed by the radio hotspots. Such broad lines reveal turbulent kinematics. For comparison, the extended ionized gas in mergers show

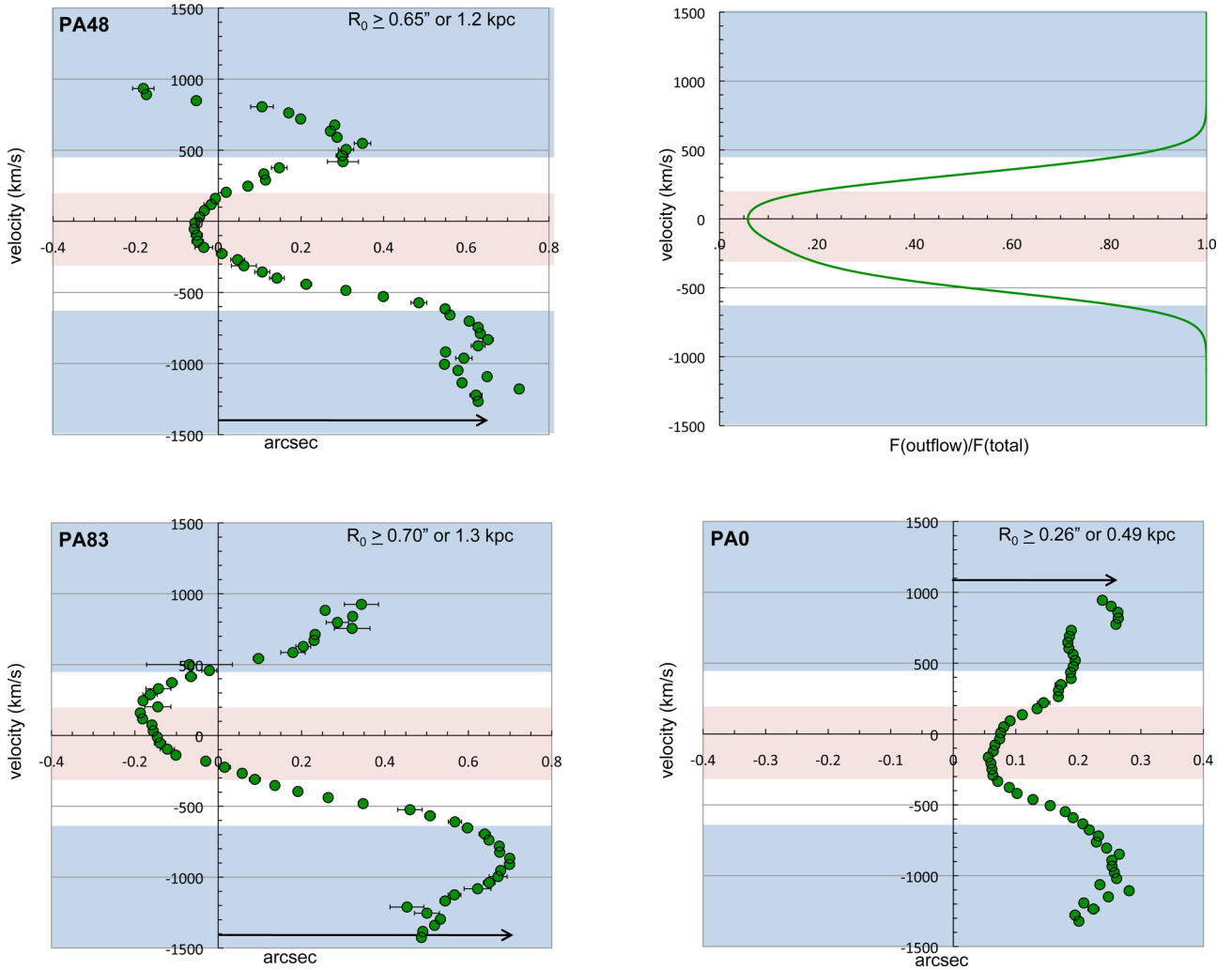


Figure 7. Spectroastrometric analysis following Villar Martín et al. (2016) along the radio hotspots axis PA48, PA83 and PA0. Left-hand panels and bottom right: shift of the spatial centroid measured for [O III] at different velocities relative to the continuum centroid along the three PAs. Top-right: velocity shift versus the relative contribution of the outflowing gas to the total [O III] line flux $\frac{F_{\text{outflow}}}{F_{\text{total}}}$. The blue areas mark the range of velocities for which the outflow dominates the line flux ($\frac{F_{\text{outflow}}}{F_{\text{total}}} \geq 0.8$). The red areas mark the velocities for which its contribution is minimum ($\frac{F_{\text{outflow}}}{F_{\text{total}}} \leq 0.2$). The emission at velocities dominated by the outflow are in general shifted relative to the continuum centroid. The arrow marks the assumed spatial shift representing the lower limit for the radial size of the outflow R_0 . The top right plot is almost identical along the three slit PAs.

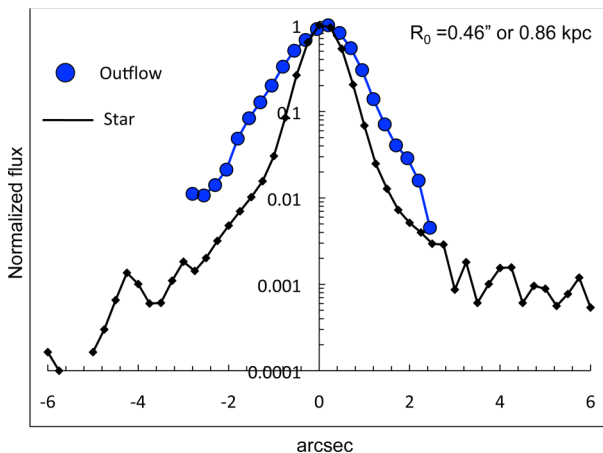


Figure 8. Comparison of the nuclear outflow spatial distribution along PA48 with the seeing profile. The outflow is spatially resolved and has $R_0 = 0.86 \pm 0.07$ kpc, corrected for seeing broadening.

typical FWHM < 250 km s $^{-1}$ even in the most dynamically disturbed systems with signs of AGN activity (Bellocchi et al. 2013; Arribas et al. 2014).

The split components are confirmed and clearly seen in the 2D PA 140 extranuclear spectrum (Fig. 10) at the location where the slit intersects the radio axis (see also Fig. 11, right-hand panels). Turbulent kinematics are detected not only along the radio axis but also at locations far from it. As an example, FWHM = 392 ± 27 and 344 ± 74 km s $^{-1}$ for apertures L and M along PA140, which trace circumgalactic gas at ~ 8 and 25 kpc from the radio axis in the perpendicular direction. Higher S/N spectra may reveal that the large FWHM are due to two split kinematic components.

The velocity curve of the turbulent gas along the radio axis (Fig. 11, left) shows a change in V_s , $|\Delta V_s| = 119 \pm 23$ km s $^{-1}$, from blueshifted in the SW to redshifted in the NE. As discussed in Section 3.1, the radio orientation places the inner jet and SW radio hotspot closer to the observer. The kinematic behaviour of the circumgalactic turbulent gas suggests that it is expanding in an

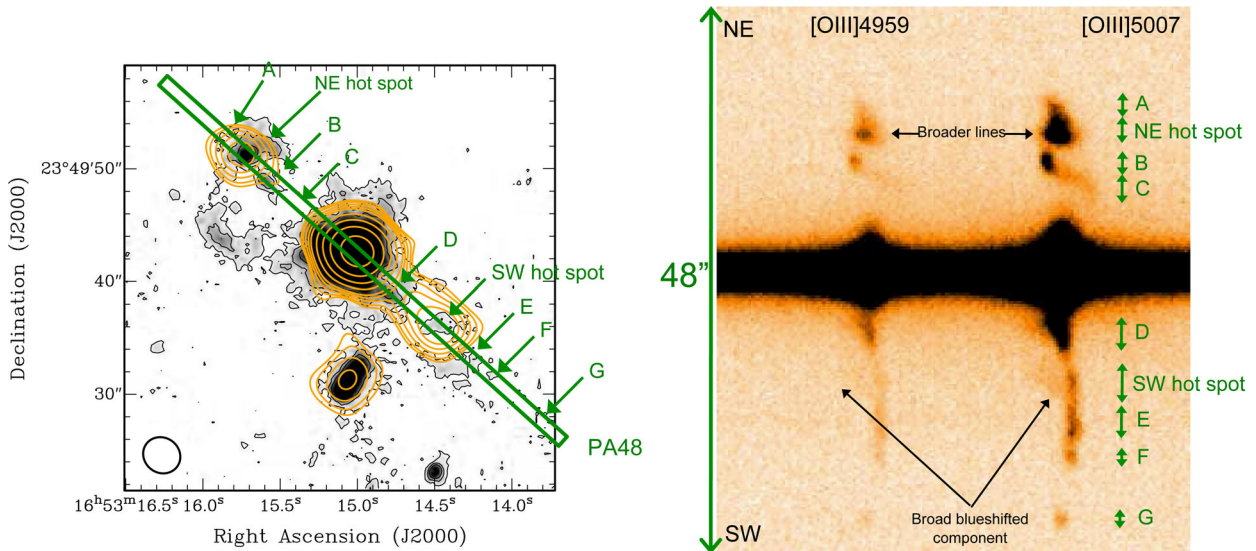


Figure 9. Left: $H\alpha$ (continuum subtracted) image and VLA radio map overlay (see Fig. 4). The PA48 slit is indicated and the main emission line features isolated in the long-slit spectrum. Right: GTC long-slit spectrum covering the $[O\text{ III}]\lambda\lambda 4959, 5007$ spectral window. 1D spectra were extracted from the apertures indicated in the figure. The lines show distinct kinematics at the location of the radio hotspots. They are broader coinciding with the NE hotspot and a broad blueshifted wing is detected at the location of the SW hotspot.

outflow, with the NE gas moving away and the SW gas moving towards the observer.

The narrow component presents the opposite behaviour (from more redshifted in the SW to more blueshifted in the NE). The scenario where this component is emitted by gas on the far side of the expanding bubbles while the broad component is emitted by the near side seems unlikely. It is not clear why both sides would emit lines with different FWHM and ionization level (see below). A more natural explanation is that the narrow component is emitted by a gas reservoir unaffected by the radio structures. This is supported by the lack of any apparent correlation in either the spatial distribution or the kinematics of this narrow component with the radio structures. In this scenario, its velocity curve suggests that it may be infalling gas.

The ionization level as traced by $[O\text{ III}]/H\beta$ presents minimum values for the turbulent gas at the hotspots (Fig. 11, left), where $[O\text{ III}]/H\beta \sim 3.7\text{--}5.7$ compared with $\sim 9.2\text{--}9.8$ for the narrow component.

Along PA83, the eastern bubble (aperture H, Fig. 10) has $\text{FWHM} = 197 \pm 16 \text{ km s}^{-1}$ and $[O\text{ III}]/H\beta = 6.8 \pm 0.7$. The profiles are slightly asymmetric with a red excess. The inner knot (aperture I) has similar $\text{FWHM} = 219 \pm 15 \text{ km s}^{-1}$, also with a slight red excess, and $[O\text{ III}]/H\beta = 8.4 \pm 1.2$. The similarity of the FWHM and $[O\text{ III}]/H\beta$ ratio compared with aperture A along PA48 are consistent with these regions being part of the same structure, as shown by the $H\alpha$ image.

We shall discuss in Section 4 how all the above results are natural consequences of the interaction between the radio structures with the ambient circumgalactic gas, which is compressed and kinematically perturbed in the process.

3.3.3 Physical properties and excitation mechanism

Different line ratios measured with the 1D spectra extracted from prominent features along PA48 and PA83 were used to investigate the excitation mechanism and physical properties of the circumgalactic gas. In addition to the NE hotspot (PA48) and the eastern bubble (aperture H, PA83, Fig. 10), a spectrum was extracted along PA48 from a large aperture covering the location of the SW radio

hotspot and apertures E and F. Relevant line ratios are shown in Table 5.

The $[S\text{ II}]$ doublet implies $n_e = 184^{+60}_{-54} \text{ cm}^{-3}$ at the NE hotspot location (Table 5). Interestingly, the temperature T_e implied by the $[O\text{ III}]\lambda\lambda 4959, 5007/[O\text{ III}]\lambda 4363$ ratio corrected for reddening with $H\alpha/H\beta$ implies $T_e = 24\,000^{+27\,800}_{-5600} \text{ K}$. The observed, uncorrected ratio sets a lower limit $T_e = 19\,000^{+1500}_{-1200}$, also rather high.

We show in Fig. 12 three standard BPT (Baldwin et al. 1981) diagnostic diagrams often used to discriminate between different types of galaxies according to Kewley et al. (2006): $H\text{ II}$ -region-type, LINERS, Seyferts and composite AGN- $H\text{ II}$. For the ‘Beetle’, the different apertures are in general located in the ‘Seyfert’ area of the diagram, implying a dominant contribution of an excitation mechanism harder than stellar photoionization. Photoionization by the quasar continuum and shock-related mechanisms (Dopita & Sutherland 1996) are natural possibilities. This is confirmed by the detection of strong $\text{He II}\lambda 4686$ at the location of the NE hotspot with $\text{He II}/H\beta = 0.17 \pm 0.03$, which is inconsistent with stellar photoionization and typical of AGNs.

We can check whether the AGN can provide sufficient photons to explain the line luminosities of the circumgalactic gas. The total $H\alpha$ luminosity of the NE bubble as measured from the narrow band image is $L_{H\alpha} \sim 1.7 \times 10^{41} \text{ erg s}^{-1}$. Correcting for reddening, assuming an average $H\alpha/H\beta \sim 4.1$ (Table 5), an intrinsic $L_{H\beta} \sim 1.3 \times 10^{41} \text{ erg s}^{-1}$ is derived. The ionizing photon luminosity required to power it is $Q_{\text{ion}}^{\text{abs}} = \frac{L_{H\beta}}{h\nu_{H\beta}} \frac{\alpha_B}{\alpha_{H\beta}^{\text{eff}}} = 5.1 \times 10^{53} \text{ s}^{-1}$ (Osterbrock 1989) where $Q_{\text{ion}}^{\text{abs}}$ is the ionizing photon luminosity absorbed by the gas, $\alpha_B = 2.5 \times 10^{-13} \text{ cm}^3 \text{ s}^{-1}$, $\alpha_{H\beta}^{\text{eff}} = 1.6 \times 10^{-14} \text{ cm}^3 \text{ s}^{-1}$ for $T_e \sim 2.0 \times 10^4 \text{ K}$ as implied by the $[O\text{ III}]$ lines and $h\nu_{H\beta}$ is the energy of an $H\beta$ photon. The NE bubble subtends an angle of $\sim 90^\circ$ on the plane of the sky around the AGN. Assuming its shape is roughly symmetric along and perpendicular to the line of sight, the necessary isotropic output from the AGN is $Q_{\text{ion}}^{\text{AGN}} = 3.5 \times 10^{54} \text{ s}^{-1}$.

The AGN ionizing luminosity can be estimated from $L_{\text{ion}}^{\text{AGN}} \sim 0.35 \times L_{\text{bol}} = 3.9 \times 10^{45} \text{ erg s}^{-1}$ (Stern, Laor & Baskin 2014).

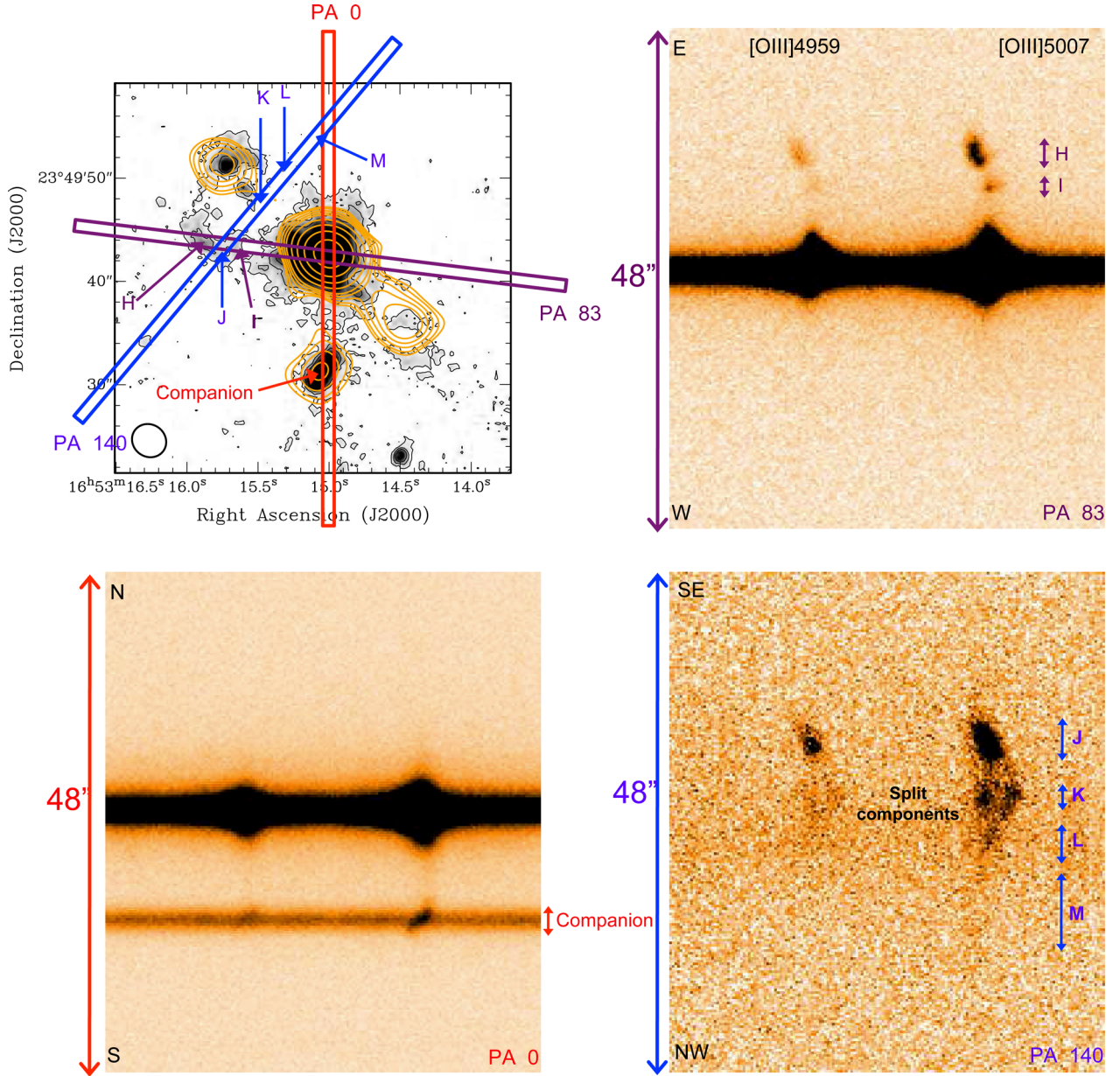


Figure 10. Top-left: the slits PA83, PA0 and PA140 (avoiding the nucleus) are shown. The apertures used in our study are indicated in the 2D [O III] spectra. Note the split components in aperture K along PA140, at the location of the radio axis (bottom right panel).

Table 4. Maximum [O III] total spatial extension D_{\max} and maximum extension R_{\max} from the galaxy continuum centroid along the four slit PAs. R_{\max} is quoted only for the three PAs that cross the galactic nucleus. The direction of R_{\max} from the continuum centroid is given in the last column.

PA	D_{\max} (kpc)	R_{\max} (kpc)	Direction
48°	71	41	SW
83°	23	23	E
0°	29	29	N
140°	43		

Assuming $L_{\nu} \propto \nu^{\xi}$, with $\xi = -1.5$, gives $Q_{\text{ion}}^{\text{AGN}} \sim 5.0 \pm 10^{55} \text{ s}^{-1}$. This is thus sufficient to explain the $\text{H}\alpha$ luminosity of the circumgalactic structures (including the SW ones, which are significantly fainter), provided they have low opacity within their volume.

On the other hand, the clear correlation between the optical and the radio morphologies suggests that shocks induced by the interaction with the radio structures contribute to the emission, at least at certain locations. This may also explain the very high T_e at the NE hotspot location.

4 DISCUSSION

We discuss in this section the nature of the large-scale outflow mechanism and the origin of the circumgalactic gas around the ‘Beetle’.

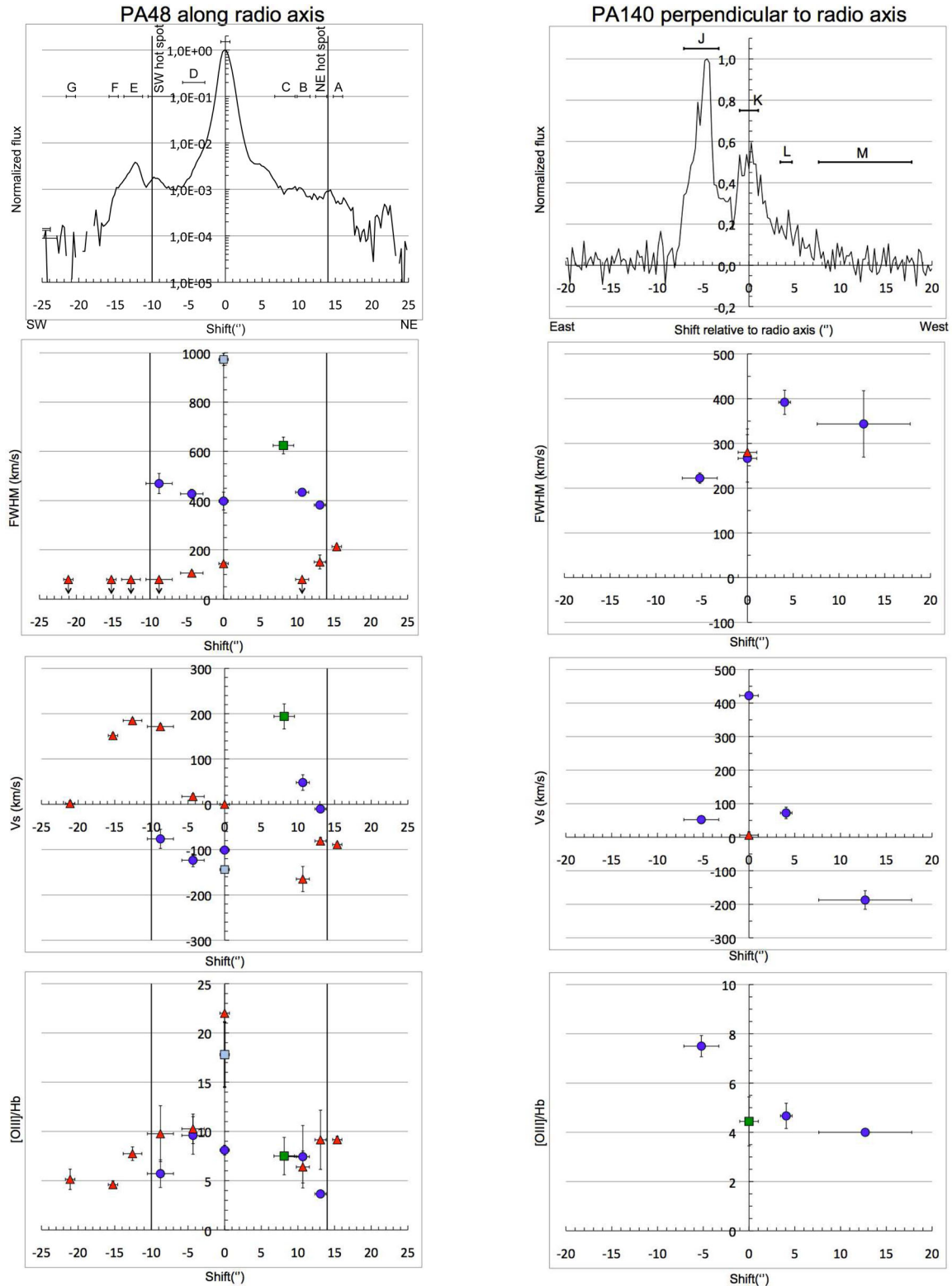


Figure 11. Spatial variation of the kinematic and ionization properties of the ionized gas. Left: from top to bottom the panels show the spatial distribution of the [O III] flux, FWHM, V_s and [O III]/H β along the radio axis (left). Blue is used for the broadest component (outflowing gas) and red for the narrowest (ambient gas). Right: same plots, but along PA140. The spatial zero marks the location of the radio axis. Green squares are used when the lines ([O III] and/or H β) appear double peaked but only one component could be fitted due to the low S/N of the spectrum. The capital letters on the top panel represent the apertures identified in Figs 9 and 10.

Table 5. Line ratios for the NE hotspot, the eastern bubble and the circumgalactic gas SW of the QSO2 along PA48. n_e and T_e could only be measured for the NE hotspot. T_e has been calculated using the measured $[\text{O III}]5007/[\text{O III}]4363$ ratio^a (which gives a lower limit on T_e), and the reddening corrected ratio^b based on $\text{H } \alpha/\text{H } \beta$. Note the very high T_e .

Ratio	NE hotspot PA48	Eastern bubble Ap. H, PA83	Large aperture PA 48 SW hotspot + Ap. E + Ap. F
$[\text{O III}]5007/\text{H } \beta$	3.9 ± 0.4	7.3 ± 0.4	6.8 ± 2.3
$[\text{N II}]6583/\text{H } \alpha$	0.27 ± 0.03	$\lesssim 0.12$	0.30 ± 0.08
$[\text{S II}]6716,6731/\text{H } \alpha$	0.58 ± 0.02	0.21 ± 0.04	0.20 ± 0.05
$[\text{O I}]6300/\text{H } \alpha$	0.17 ± 0.03	0.09 ± 0.01	$\lesssim 0.13$
$\text{H } \gamma/\text{H } \beta$	0.46 ± 0.06	0.44 ± 0.05	
$\text{H } \alpha/\text{H } \beta$	5.3 ± 0.6	2.7 ± 0.4	5.3 ± 1.8
$\text{He II}4686/\text{H } \beta$	0.17 ± 0.03		
$[\text{S II}]4068/[\text{S II}]6716,6731$	0.07 ± 0.02		
$[\text{S II}]6716/[\text{S II}]6731$	1.25 ± 0.04		
$[\text{O III}]4959,5007/[\text{O III}]4363^a$	44.3 ± 5.4		
$[\text{O III}]4959,5007/[\text{O III}]4363^b$	30.9 ± 15.8		
n_e	184^{+60}_{-54}		
T_e^a	$1.90^{+0.15}_{-0.12}$		
T_e^b	$2.40^{+2.78}_{-0.56}$		

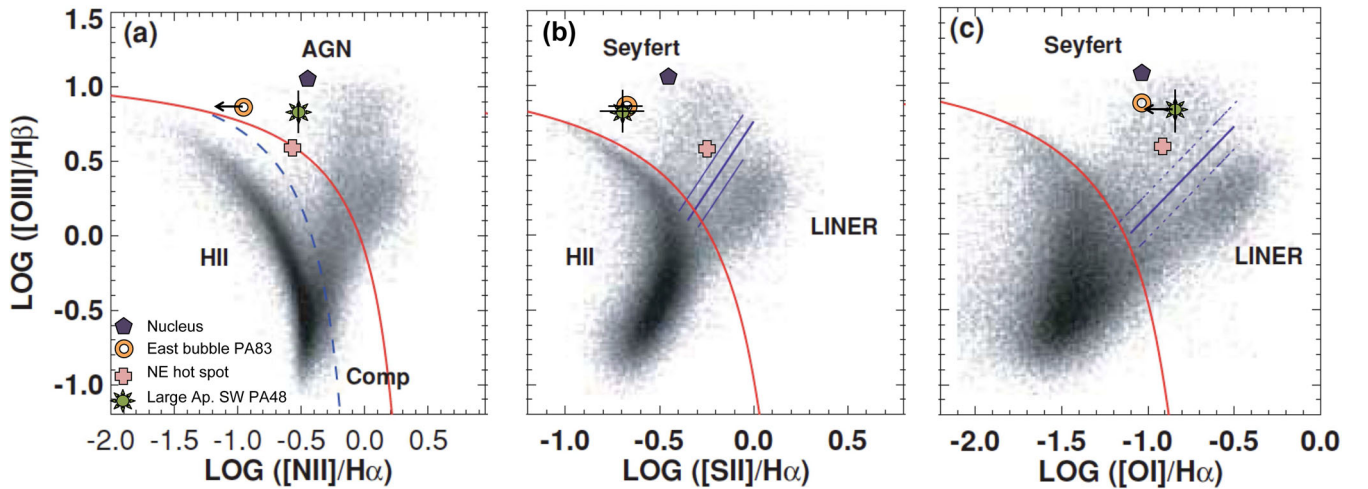


Figure 12. BPT diagnostic diagrams taken from Kewley et al. (2006) with the location of the nuclear spectrum of the ‘Beetle’, the NE hotspot, the eastern bubble (PA83) and the large aperture SW of the QSO2 along PA48. Data error-bars smaller or similar to the symbol size are not shown. The red solid line is Kewley et al. (2006) extreme starburst classification line. The blue dashed line is the Kauffmann et al. (2003) pure star formation line. The blue solid line is the Seyfert-LINER classification line. The three lines separate galaxies into H II-region-like, Seyferts, LINERS and composite AGN-H II.

4.1 Giant bubbles inflated by a nuclear AGN wind

We inferred in Section 3.2, $M_o = 3.5 \times 10^6 M_\odot$, $\dot{M}_o = 2.6 M_\odot \text{ yr}^{-1}$, $\dot{E}_o = 3.2 \times 10^{41} \text{ erg s}^{-1}$ (or $\sim 10^{-5} \times L_{\text{Edd}}$) and $\dot{p}_o = 1.0 \times 10^{34} \text{ dyne}$ (or $\sim 0.01 L_{\text{Edd}}/c$) for the nuclear outflow. If this is powered by an AGN wind, both \dot{E}_o and \dot{p}_o are well below the minimum values required to have a substantial impact on the host galaxy ($\dot{E}_o \gtrsim 0.05 L_{\text{Edd}}$ and $\dot{p}_o \gtrsim 20 L_{\text{Edd}}/c$; Zubovas & King 2012). The outflow high density ($n_e = 2571^{+14181}_{-1461} \text{ cm}^{-2}$) and small size ($R_o \lesssim 1 \text{ kpc}$) are consistent with Faucher-Giguère & Quataert (2012), who showed that such high densities would be sufficient to quench an AGN-powered wind prior to reaching radii $\gtrsim 1 \text{ kpc}$. Thus, if the nuclear-ionized outflow has been generated by an AGN wind, we find no evidence for a significant impact on the host galaxy, in agreement with Villar Martín et al. (2016) who found this to be a common situation in QSO2 at $z \lesssim 0.7$.

The arguments above are based on the assumption that the AGN-driven wind responsible for the nuclear outflow expands in a high-density medium. If on the contrary it encounters paths of less resistance with densities significantly less than the normal volume-averaged gas densities, it could advance more freely and expand to much larger distances (Nims, Quataert & Faucher-Giguère 2015; Mukherjee et al. 2016). Such scenario has been proposed, for instance, to explain the large-scale radio and optical bubbles associated with the ‘Teacup’ QSO2 (Harrison et al. 2015).

We investigate next whether such scenario could explain the properties (size, velocity and mass) of the circumgalactic optical arcs of the ‘Beetle’. Following Nims et al. (2015), the kinetic energy of the wind can be approximated as $L_{\text{kin}} \sim 0.05 \times L_{\text{bol}} \sim 5 \times 10^{44} \text{ erg s}^{-1}$. We use equations 6 and 7 in their paper to calculate the radius R_s of the forward shock of the wind and its velocity v_s . We use the same fiducial values for $R_o = 100 \text{ pc}$, $n_{\text{H},0} = 10 \text{ cm}^{-3}$, $v_{\text{in}} = 0.1 c$

and the density varying as a power law of index $\beta = 1.0$ (see Nims et al. 2015 for details). In 30 Myr, which is a reasonable quasar lifetime, the wind could create a bubble of radial size $R_s \sim 25$ kpc as observed for the ‘Beetle’. At that time, its expansion velocity will be $v_s \sim 535 \text{ km s}^{-1}$. This is in reasonable agreement with the V_s values measured for the circumgalactic gas (Figs 11), taking into account that these are line-of-sight projected velocities. It thus seems plausible that an AGN wind expanding through paths of low resistance can create the huge bubbles.

Can this mechanism eject sufficient mass? We have estimated what fraction of the gas dragged by the nuclear outflow can escape the gravitational potential of the galaxy. For this, we constrain the gas fraction that moves with velocity v higher than the escape velocity v_{esc} . v_{esc} for an isothermal sphere at a distance r is given by (Rupke, Veilleux & Sanders 2002) $v_{\text{esc}}(r) = \sqrt{2}v_c[1 + \ln(r_{\text{max}}/r)]^{1/2}$, where v_c is the circular velocity that scales with the stellar velocity dispersion σ_* as $v_c = \sqrt{2}\sigma_*$, where $\sigma_* \sim 200 \text{ km s}^{-1}$ (Section 1.1). r_{max} is unknown. We have considered three possible truncation values $r_{\text{max}} = 3, 10$ and 100 kpc. We assume $r = R_o \sim 0.86$ kpc, which is the radial size of the outflow (Section 3.2.2). v_{esc} at R_o is in the range $\sim 633\text{--}960 \text{ km s}^{-1}$ for r_{max} in the range $3\text{--}100$ kpc. Only ~ 3 per cent of the total nuclear $L_{\text{H}\beta}$ is emitted by gas moving at $v_{\text{esc}} > 633 \text{ km s}^{-1}$. Thus, the nuclear outflow can eject only $\sim 0.03 \times M_o = 10^5 M_\odot$ outside the galaxy at a rate of $\sim 0.03 \times M_o = 0.08 M_\odot \text{ yr}^{-1}$ (Section 3.2.3). These are gross upper limits, since higher v_{esc} are possible.

The total H α intrinsic (reddening corrected) luminosity of the NE bubble is $L_{\text{H}\alpha} \sim 4.0 \times 10^{41} \text{ erg s}^{-1}$. Assuming $n_e \sim 184 \text{ cm}^{-3}$ as measured at the location of the NE hotspot, the total NE bubble mass of the H α emitting gas is $\sim 2.0 \times 10^7 M_\odot$. It follows that $>3.0 \times 10^8$ yr of continuous mass ejection would have been required to create the NE bubble, which is longer than any realistic quasar episode. The inconsistency gets worse if the mass of the SW arcs is also taken into account.

Because it will be relevant in Section 4.3, we highlight here that the same conclusion applies if the nuclear outflow was triggered by the small-scale radio jet instead of an AGN wind, since the necessary time of continuous mass ejection is longer than realistic radio source ages.

4.2 Large-scale radio–gas interactions

The above scenario is also difficult to reconcile with the clear correlation between the morphological, kinematic and ionization properties of the ionized gas and the large-scale radio structures (Section 3.3.2). A more natural scenario is one in which the radio structures have been originated in the neighbourhood of the SMBH and have escaped out of the galaxy boundaries. The morphological features (distant hotspots, a diffuse lobe-like component and the inner jet-like structure in the central kpc region) are well-known constituents of the radio structures in many active galaxies. No convincing alternative explanations (see, for instance, Harrison et al. 2015) for their origin seem likely.

These structures have interacted in their advance with the *in situ* (see below) circumgalactic gas. Our preferred scenario is strongly supported by studies of radio galaxies and radio-loud quasars with clear signs of radio–gas interactions (e.g. Clark et al. 1998; Villar Martín et al. 1999; Tadhunter et al. 2000; Best, Röttgering & Longair 2001; Humphrey et al. 2006).

We have seen that (a) the line emission is enhanced at the location of the radio hotspots, especially the NE one, (b) the gas kinematics are turbulent across the spatial range circumscribed by the radio

hotspots (not beyond), (c) the turbulent gas shows minima in the ionization level at the location of the radio hotspots, (d) the gas overlapping with the NE hotspot is very hot $T_e \gtrsim 1.9 \times 10^4 \text{ K}$ and (e) there is turbulent gas not only along the radio axis (up to ~ 26 kpc from the AGN), but also far away from it (~ 25 kpc from the radio axis, in the direction perpendicular to it) (Section 3.3).

Powerful radio galaxies with radio–gas interactions at different redshifts often show close radio–optical associations, emission line flux enhancement, ionization minima and kinematic turbulence (split lines, broad components) coincident with the radio structures, anticorrelation between line FWHM and gas ionization level, high T_e have been seen in such systems. They can all be naturally explained by the interaction between the radio structures and the ambient gas. The shocks resulting from such interactions create radial outflows that drag, heat and compress the multiphase gaseous medium (Bicknell 1994; Mukherjee et al. 2016).

The presence of turbulent gas in the ‘Beetle’ up to ~ 26 kpc along the radio axis and ~ 25 kpc away from it reveals the action of the shocks across a huge volume. This has been observed also in some powerful radio galaxies (Villar Martín et al. 1999; Tadhunter et al. 2000). Turbulent kinematics up to ~ 6 kpc from the AGN have also been reported for the ‘Teacup’ radio-quiet QSO2 (Keel et al. 2017; Ramos Ramos Almeida et al. 2017). Although a scenario where the outflows have been triggered by an AGN wind (rather than by the radio structures) cannot be rejected, it is possible that a similar mechanism as the one inferred for the ‘Beetle’ is at work (Harrison et al. 2015).

Gaspari et al. (2012) have shown that a radio source of similar power as the ‘Beetle’ can create a wealth of observable features around ellipticals in poor environments, such as X-ray cavities surrounded by weak shocks, large buoyant bubbles, extended filamentary multiphase gas features (including cold gas with $T_e \lesssim 20\,000 \text{ K}$ gas) and subsonic chaotic turbulence. The effects can be visible up to several kpc from the SMBH. Whether this can occur up to ~ 26 kpc is not clear from the point of view of the simulations.

Powerful radio galaxies with large volumes of gas affected by radio-induced outflows (Villar Martín et al. 1999; Tadhunter et al. 2000), show wide area radio features (e.g. radio lobes) overlapping with the optical bubbles or bow shocks. This is not the case in the ‘Beetle’, but this is not an inconsistency of our proposed scenario. Although a relativistic jet may appear to be collimated in radio, it will in fact launch a bubble defined by the forward shock (Bicknell 1994; Mukherjee et al. 2016). Hence, although the radio contours may trace predominantly the central axis, where the electrons are relativistic and emit intense synchrotron radiation, the outer shock will be larger, more dilute and difficult to detect. This may explain why broad radio lobes overlapping with the H α bubble edges have not been detected in the ‘Beetle’. A deeper radio scan may reveal them.

We can apply the methodology of (Nims et al. 2015, see Section 4.1) to investigate whether a radio source of the same mechanical power as that of the ‘Beetle’ can inflate the huge observed bubbles. The equations were originally derived to model the expansion of a homogeneous spherically symmetric wind. While strong fast jets produce asymmetric bubbles with the jet head progressing much faster, weak jets (as that in the ‘Beetle’) evolve more spherically (Mukherjee et al. 2016). We thus consider the equations valid as well in the scenario where the outflow has been induced by the radio source. The mechanical power of the radio source can be calculated as $P_{\text{jet}} \sim 5.8 \times 10^{43} (P_{\text{radio}}/10^{40})^{0.70} \text{ erg s}^{-1}$ (Cavagnolo et al. 2010). For the ‘Beetle’, we infer $P_{\text{radio}} = 9.1_{-5.9}^{+45.3} \times 10^{40} \text{ erg s}^{-1}$ using the radio power at 1.4 GHz, integrating between 10 MHz and 30 GHz,

considering the range of expected spectral index $\alpha = 0.094_{-1.01}^{+0.76}$ and $F_{\nu} \propto \nu^{\alpha}$. Hence, $P_{\text{jet}} = 2.7_{-1.4}^{+6.8} \times 10^{44} \text{ erg s}^{-1}$. In 35 Myr, which is a reasonable radio source age (Parma et al. 1999), the jet could therefore create a bubble of radial size $R_s \sim 25 \text{ kpc}$. At that time, its expansion velocity will be $v_s \sim 442 \text{ km s}^{-1}$.

4.3 The origin of the circumgalactic gas

As we saw in Section 4.1, it is unlikely that the circumgalactic features consist of gas ejected from the galaxy by the nuclear outflow, independently of whether this has been triggered by an AGN wind or the small-scale radio jet. It appears more likely that they consist of *in situ* gas, maybe tidal remnants redistributed during galactic interactions across $\sim 71 \text{ kpc}$ (Section 3.3.1), as observed. Such events are expected to populate the CGM with tidal debris. The circumgalactic gas around the ‘Beetle’ has been shaped and rendered visible due to the illumination by the QSO and the action of the radio-induced outflows. The possible detection of an infalling circumgalactic reservoir of gas (Section 3.3.2) could point to a scenario in which part of the CGM is raining back, falling towards the gravitational centre probably defined by the QSO2 host.

4.4 Is the ‘Beetle’ related to high-excitation radio galaxies?

The novelty of our results lies on the fact that the ‘Beetle’ is radio quiet. As explained in Section 1, radio-induced feedback has been rarely considered as potentially relevant in radio-quiet luminous AGNs, especially across large spatial scales (\gg several kpc). In this section, we analyse in more depth the implications of our results, by comparing the ‘Beetle’ with radio galaxies.

Radio galaxies can be classified into two distinct classes according to the optical emission line ratios and the [O III] $\lambda 5007$ equivalent width: high- (HERG) and low-excitation (LERG) radio sources, which show profound differences (e.g. Laing et al. 1994; Tadhunter et al. 1998; Best & Heckman 2012). Contrary to LERG, HERG have high-luminosity accretion discs (+ X-ray corona), bright line emission, NIR/sub-mm evidence of dusty obscuring torus and orientation-dependent properties. Some fundamental differences have been interpreted in terms of differences on the underlying accretion modes. In HERG, accretion at high Eddington ratios proceeds via a geometrically thin, optically thin accretion disc with a high radiative efficiency, while LERG are powered by advection-dominated accretion flows (Narayan & Yi 1994) with low radiative efficiency. Hardcastle, Evans & Croston (2007) show that LERG are predominantly low-power Fanaroff–Riley class I (FR-I) sources, while the HERG population consists of both FR-I and the more powerful FR-II sources, whose relativistic jets end in bright hotspots. The dominant feedback mechanism is also thought to be clearly distinct between LERG and HERG. LERG are dominated by radio-mode feedback, where the bulk of the energy is ejected in kinetic form through radio jets (e.g. Croton et al. 2006) and efficiently coupled to the galaxies’ gaseous environment (Best et al. 2006). The radiative (or quasar) mode is thought to dominate in HERG.

How does the ‘Beetle’ fit into this picture? Based on its optical spectroscopic properties, the ‘Beetle’ is indistinguishable from HERG (Fig. 13). It has a very high excitation index (Best & Heckman 2012) $EI = \log_{10}([\text{O III}]/\text{H}\beta) - \frac{1}{3}[\log_{10}([\text{N II}]/\text{H}\alpha) + \log_{10}([\text{S II}]/\text{H}\alpha) + \log_{10}([\text{O I}]/\text{H}\alpha)] = 1.70$, significantly higher than the limiting value 0.95 proposed by Best & Heckman (2012) to separate LERG and HERG. Indeed, it is at the high end of $\text{EW}_{[\text{O III}]\lambda 5007} = 430 \text{ \AA}$ (rest-frame value) and EI values spanned by

the radio galaxy sample studied by these authors. It has an Eddington ratio $\lambda = \frac{L_{\text{bol}}}{L_{\text{Edd}}} = 0.33$ (Section 1.1). The transition between the radiatively efficient accretion regime and the radiatively inefficient accretion regime typically occurs around $\lambda \sim 0.01$, i.e. 1 per cent of the Eddington rate, below which, the kinetic output dominates over the radiative output. The ‘Beetle’ is accreting at a very high rate. In fact, few radio galaxies accrete at such high rates (Best & Heckman 2012; Sikora et al. 2013; Ishibashi et al. 2014).

The rest-frame radio power of the ‘Beetle’ ($\log(P_{1.4\text{GHz}}) = 30.2$ in $\text{erg s}^{-1} \text{ Hz}^{-1}$), although modest, is within the range measured in radio galaxies. A critical difference is that its very high bolometric luminosity makes it a radio-quiet system. HERG of similar $L_{[\text{O III}]}$ show \gtrsim several $\times 100$ times more powerful radio sources (Fig. 13, left). Following Ishibashi et al. (2014), we define the radio-loudness parameter $R' = \frac{L_{1.4\text{GHz}}}{L_{[\text{O III}]}}$, where $L_{1.4\text{GHz}}$ is the rest-frame luminosity at 1.4 GHz. For the ‘Beetle’ $\log(R') = -2.78$ below the range spanned by radio galaxies (both HERG and LERG). These objects show $\log(R') \gtrsim -2.5$ (Best & Heckman 2012; Ishibashi et al. 2014).

LERG and HERG show an anticorrelation between $\log(R')$ and $\log(\lambda')$ where the new accretion rate $\lambda' = 3500 \times \frac{L_{[\text{O III}]}}{L_{\text{Edd}}} = 0.42$ is calculated in coherence with Ishibashi et al. (2014).⁷ This is likely a result of either an enhancement of the radio jet emission at low accretion rate and/or a decrease in the optical emission due to the decline of the radiative efficiency in the radiatively inefficient accretion flow mode. The best fit is different for HERG and LERG (Buttigione et al. 2010; Ishibashi et al. 2014), being much steeper for the former. For the ‘Beetle’, $\log(\lambda') = -0.37$ and $\log(R') = -3.28$. All uncertainties considered, including the scatter of the correlations, these values are consistent with the HERG fit (expected $\log(R') = -2.6$) and inconsistent with the LERG fit (expected $\log(R') = -0.65$).

Interestingly, the ‘Teacup’ is very similar to the ‘Beetle’ in numerous aspects. It is also a radio-quiet luminous QSO2 hosted by a bulge-dominated system. It shows prominent shells indicative of previous merger activity. The axis of the radio and optical bubbles (~ 10 – 12 kpc in size) runs roughly perpendicular to the main shells axis, as in the ‘Beetle’ (Keel et al. 2012; Harrison et al. 2015; Ramos Ramos Almeida et al. 2017) and the large-scale outflow may also have been triggered by the radio structures (Harrison et al. 2015). We have used the following information published in the literature: the optical nuclear line ratios (Keel et al. 2012), $L_{[\text{O III}]} = 3.8 \times 10^{43} \text{ erg s}^{-1}$, $\log(P_{1.4\text{GHz}}) = 30.2$ in $\text{erg s}^{-1} \text{ Hz}^{-1}$ (Harrison et al. 2015), $\log(M_{\text{BH}}) = 8.4$, indirectly inferred from the bulge stellar mass $\log(M_{\text{sph}}/M_{\odot}) = 10.8$ (VizieR catalogue, based on Simard et al. 2011). We obtain $EI = 1.52$, $\log(\lambda') = -0.10$ and $\log(R') = -3.16$, i.e. very high excitation index, very high accretion rate and very low radio-loudness parameter, demonstrative of its radio quietness (Fig. 13). As for the ‘Beetle’, these values are consistent with the extrapolation of the $\log(R')$ versus $\log(\lambda')$ correlation of HERG into the radio-quiet regime and inconsistent with the LERG correlation.

The properties of the ‘Beetle’ and the ‘Teacup’ suggest that they are high-excitation radio-quiet QSO2 that are similar to the population of HERG, extended into the regime of very high accretion efficiencies and modest radio luminosities, i.e. the radio-quiet regime. This is consistent with Lacy et al. (2001) who proposed that there is a continuous variation of radio luminosity in quasars and there is

⁷ The authors assume $L_{\text{bol}} = 3500 \times L_{[\text{O III}]}$ following Heckman et al. (2004).

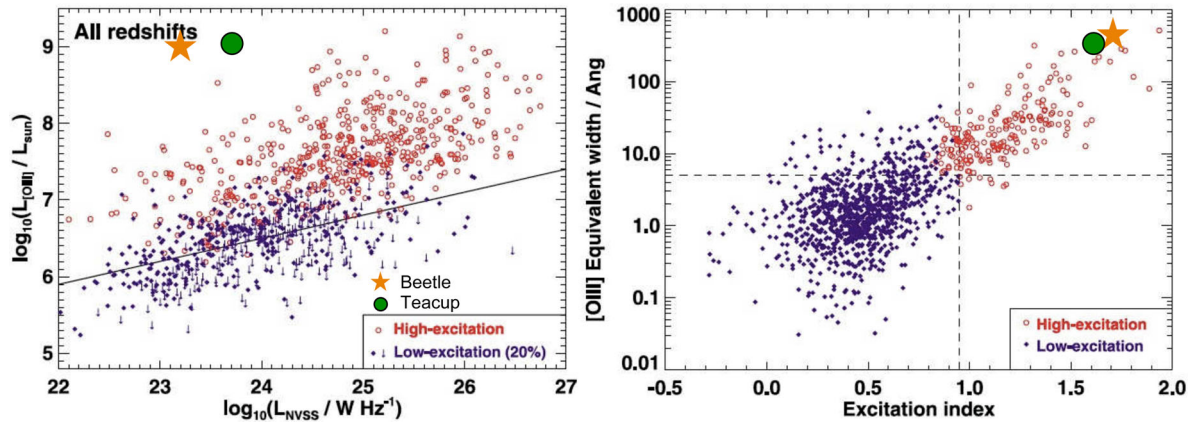


Figure 13. Figs 1 and 2 from Best & Heckman (2012) showing the location of the ‘Beetle’ (beige star) in comparison with HERG and LERG. The ‘Teacup’ (Harrison et al. 2015) is also shown (green circle). From the optical spectroscopic point of view, both objects are like HERG with rather extreme values of both [O III] λ 5007 equivalent width and excitation index (right). Their relatively low radio luminosity, on the other hand, places them well above the sequence defined by the radio galaxy sample in the left diagram.

no evidence of a ‘switch’ at some set of critical parameter values that turns on powerful radio jets.

Based on the very high accretion rate and the radio quietness (or very low R'), radiative feedback would be expected to play a dominant role in both objects. We have seen, however, that although this mechanism cannot be discarded in the central region near the AGN ($\lesssim 1$ kpc), the radio-induced feedback dominates the ‘Beetle’ (maybe also the ‘Teacup’) across a huge volume of many tens of kpc in size, reaching regions well outside the galaxy boundary and into the CGM. This opens the possibility that the radio-mode feedback may contribute to the re-heating of the cooling gas in massive galaxies not only in radio-loud systems (Best et al. 2006), but also in at least some radio-quiet AGNs.

5 SUMMARY AND CONCLUSIONS

We have presented a detailed study of the ‘Beetle’, a radio-quiet QSO2 at $z = 0.103$, based on GTC optical images and long-slit spectroscopy as well as VLA radio maps.

(i) The ‘Beetle’ shows clear morphological signs of a tidal interaction (shells, filaments), probably with a star-forming companion galaxy located at ~ 20 kpc. The system is associated with a spectacular set of circumgalactic ionized knots and three arcs reminiscent of optical bow shocks or bubbles, with a main axis aligned with the radio axis. They are located at 19, 25 and 26 kpc from the AGN. The maximum total extension of the ionized gas is measured along the radio axis (~ 71 kpc), with maximum extension from the QSO2 ~ 41 kpc. These circumgalactic features are ionized by shocks and/or the quasar continuum.

(ii) The radio map has revealed the existence of a previously unknown extended radio source, with a central jet ~ 4.3 kpc long and two hotspots separated by ~ 46 kpc, well outside the galaxy boundaries. The inner jet and the outer radio axis form a 19° angle, which would indicate a substantial precession of the radio jet or its bending as it propagates outward.

(iii) The morphological, ionization and kinematic properties of the large-scale ionized gas are correlated with the radio structures. We have seen that (a) the line emission is enhanced at the location of the radio hotspots, especially the NE one, (b) gas kinematic turbulence (FWHM ~ 380 – 470 km s^{-1}) is detected across the spatial

range circumscribed by the radio hotspots (not beyond), (c) the turbulent gas shows minima in the ionization level at the location of the radio hotspots, (d) the gas overlapping with the NE hotspot is very hot $T_e \gtrsim 1.9 \times 10^4$ K and (e) there is turbulent gas not only along the radio axis (up to ~ 26 kpc from the AGN), but also far away from it (~ 25 kpc from the radio axis, in the direction perpendicular to it). In addition, a reservoir of more quiescent gas has also been detected whose kinematic pattern suggests infall.

(iv) We propose the following scenario: the interaction between the QSO2 host and the nearby companion galaxy has redistributed galactic material (stars and gas) across ~ 70 kpc, at opposite sides of both galaxies. Part of the gas is in the process of falling towards the gravitational centre, probably defined by the QSO2 host. The radio structures have escaped from the vicinity of the active nucleus out into the CGM. They interact with the gas located in their path. Shocks drag, heat and compress the multiphase medium within a huge volume enhancing the line emission, perturbing the kinematics and changing the physical properties up to ~ 25 kpc along the radio axis and perpendicular to it. Our preferred scenario is strongly supported by studies of radio galaxies and radio-loud quasars at different redshifts with clear signs of radio–gas interactions.

(v) Specific 3D hydrodynamic simulations of interactions between AGN jets and the multiphase ISM adapted to the ‘Beetle’ would be of great value to quantify accurately how radio-induced feedback is affecting its large-scale environment in terms of energy injection, heating and mass ejection. Ultimately, this would show whether the radio-induced feedback can have a significant impact on the evolution of the QSO2 host by means of quenching star formation and/or ejecting a significant fraction of the galaxy ISM.

(vi) Large-scale effects (\gg several kpc) of the radio-induced feedback in radio-quiet AGNs are usually not expected. Our results demonstrate that this idea needs to be reconsidered. We have found that jets of modest power can remain strong enough in radio-quiet objects for length-scales of tens of kpc to interact with the galactic and circumgalactic environment and provide a feedback mechanism that can affect huge volumes in and around galaxies.

(vii) The radio and optical properties of the ‘Beetle’ imply a very high accretion index, very high accretion rate and a very low radio-loudness parameter compared with HERG. We propose that the ‘Beetle’ (possibly also the famous ‘Teacup’ radio-quiet QSO2 at $z \sim 0.085$; Keel et al. 2012; Gagne et al. 2014) are high-excitation

radio-quiet QSO2 which are similar to the population of HERG, extended into the radio-quiet regime of objects with high bolometric luminosities and low or moderate radio luminosities. The ‘Beetle’ demonstrates that jets of modest power can be the dominant feedback mechanism acting across huge volumes in highly accreting luminous radio-quiet AGNs, where radiative (or quasar) mode feedback would be expected to dominate.

ACKNOWLEDGEMENTS

This work is based on observations carried out at the Observatorio Roque de los Muchachos (La Palma, Spain) with OSIRIS on GTC (programmes GTC37/14A, GTC1/15A and GTC01-16ADDT) and the Very Large Array (programmes VLA/15A-237 and VLA/16A-088). Partly based on observations made with the GTC telescope, under Director’s Discretionary Time. We thank the GTC staff for their support with the optical imaging and spectroscopic observations and the VLA staff for executing the radio observations. Thanks to Gustaaf van Moorsel for his valuable advice about the radio observations.

MVM, AC and BE acknowledge support from the Spanish Ministerio de Economía y Competitividad through the grants AYA2015-64346-C2-2-P and AYA2012-32295. AH acknowledges Fundação para a Ciência e a Tecnologia (FCT) support through UID/FIS/04434/2013, and through project FCOMP-01-0124-FEDER-029170 (Reference FCT PTDC/FIS-AST/3214/2012) funded by FCT-MEC (PIDDAC) and FEDER (COMPETE), in addition to FP7 project PIRSES-GA-2013-612701. AH also acknowledges a Marie Curie Fellowship co-funded by the FP7 and the FCT (DFRH/WIIA/57/2011) and FP7 / FCT Complementary Support grant SFRH/BI/52155/2013. BE acknowledges support from the European Union 7th Framework Programme (FP7-PEOPLE-2013-IEF) under grant 624351. CRA acknowledges the Ramón y Cajal Programme of the Spanish Ministry of Economy and Competitiveness through project RYC-2014-15779 and the Spanish Plan Nacional de Astronomía y Astrofísica under grant AYA2016-76682-C3-2-P.

This research has used the following: (1) The VizieR catalogue access tool, CDS, Strasbourg, France. The original description of the VizieR service was published in Ochsenbein et al. (2000). (2) The NASA/IPAC circumgalactic Database (NED) that is operated by the Jet Propulsion Laboratory, California Institute of Technology, under contract with the National Aeronautics and Space Administration. (3) Data from Sloan Digital Sky Survey. Funding for the SDSS and SDSS-II has been provided by the Alfred P. Sloan Foundation, the Participating Institutions, the National Science Foundation, the U.S. Department of Energy, the National Aeronautics and Space Administration, the Japanese Monbukagakusho, the Max Planck Society and the Higher Education Funding Council for England. The SDSS Web Site is <http://www.sdss.org/>.

REFERENCES

Alatalo et al., 2014, *ApJ*, 798, 31
 Arribas S., Colina L., Bellocchi E., Maiolino R., Villar Martín M., 2014, *A&A*, 568, 14
 Athanassoula E., Bosma A., 1985, *ARA&A*, 23, 147
 Baldwin J., Philips M., Tevich R., 1981, *PASP*, 93, 5
 Bellocchi E., Arribas S., Colina L., Miralles-Caballero D., 2013, *A&A*, 557, 59
 Bennert N., Jungwiert B., Komossa S., Haas M., Chini R., 2006a, *A&A*, 456, 953

Bennert N., Jungwiert B., Komossa S., Haas M., Chini R., 2006b, *A&A*, 459, 55
 Best P. N., Heckman T. M., 2012, *MNRAS*, 421, 1569
 Best P. N., Röttgering H. J. A., Longair M. S., 2001, *MNRAS*, 311, 23
 Best P. N., Kaiser C. R., Heckman T. M., Kauffmann G., 2006, *MNRAS*, 368, L67
 Bicknell G. V., 1994, *ApJ*, 422, 542
 Briggs D. S., 1995, PhD thesis, New Mexico Institute of Mining and Technology
 Buttiglione S., Capetti A., Celotti A., Axon D. J., Chiaberge M., Macchetto F. D., Sparks W. B., 2010, *A&A*, 509, 6
 Carniani S. et al., 2015, *A&A*, 598, 102
 Cavagnolo K. W., McNamara B. R., Nulsen P. E. J., Carilli C. L., Jones C., Bîrzan L., 2010, *ApJ*, 720, 1066
 Clark N. E., Axon D. J., Tadhunter C. N., Robinson A., O’Brien P., 1998, *ApJ*, 494, 546
 Croton D. J. et al., 2006, *MNRAS*, 365, 11
 Di Matteo T., Springel V., Hernquist L., 2005, *Nature*, 433, 604
 Dopita M., Sutherland R., 1996, *ApJS*, 102, 161
 Duc P. A. et al., 2015, *MNRAS*, 446, 120
 Fabian A. C., 2012, *ARA&A*, 50, 455
 Fanaroff B. L., Riley J. M., 1974, *MNRAS*, 167, 31
 Fauchier-Giguère C. A., Quataert E., 2012, *MNRAS*, 425, 605
 Ferrarese L., Merritt D., 2000, *ApJ*, 539, L9
 Förster Schreiber N. M. et al., 2014, *ApJ*, 787, 38
 Fu H., Stockton A., 2009, *ApJ*, 690, 953
 Gagne J. P. et al., 2014, *ApJ*, 792, 72
 Gaspari M., Brighenti F., Temi P., 2012, *MNRAS*, 424, 190
 González J. J., Cepa J., González Serrano J. I., Sánchez Portal M., 2014, *MNRAS*, 443, 3289
 Greene J. E., Zakamska N., Ho L., Barth A., 2011, *ApJ*, 732, 9
 Guillard P. et al., 2012, *ApJ*, 747, 95
 Hakobyan A. A. et al., 2009, *ApJ*, 52, 40
 Hardcastle M. J., Evans D. A., Croston J. H., 2007, *MNRAS*, 376, 1849
 Harrison C. M. et al., 2012, *MNRAS*, 426, 1073
 Harrison C. M., Alexander D. M., Mullaney J. R., Swinbank A. M., 2014, *MNRAS*, 441, 3306
 Harrison C. M., Thomson A. P., Alexander D. M., Bauer F. E., Edge A. C., Hogan M. T., Mullaney J. R., Swinbank A. M., 2015, *ApJ*, 800, 45
 Heckman T., Kauffmann G., Brinchmann J., Charlot S., Tremonti S., White S. D. M., 2004, *ApJ*, 613, 109
 Helou G., Soifer B. T., Rowan-Robinson M., 1985, *ApJ*, 298, L7
 Holt J., Tadhunter C. N., Morganti R., Emonts B., 2011, *MNRAS*, 410, 1527
 Humphrey A., Villar Martín M., Fosbury R., Vernet J., di Serego Alighieri S., 2006, *MNRAS*, 369, 1103
 Husemann B., Wisotzki L., Sánchez S. F., Jahnke K., 2013, *A&A*, 549, 43
 Husemann B., Scharwaechter J., Bennert V. N., Mainieri B., Woo J.-H., Kakkad D., 2016, *A&A*, 594, 44
 Ishibashi W., Auger M. W., Zhang D., Fabian A. C., 2014, *MNRAS*, 443, 1339
 Karouzos M., Woo J. H., Bae H. J., 2016, *ApJ*, 819, 148
 Kauffmann G. et al., 2003, *MNRAS*, 341, 54
 Keel W. C. et al., 2012, *MNRAS*, 420, 878
 Keel W. C. et al., 2017, *ApJ*, 835, 256
 Kellermann K. I., Sramek R. A., Schmidt M., Green R. F., Shaffer D. B., 1994, *AJ*, 108, 1163
 Kennicutt R. C., Jr, 1998, *ARA&A*, 36, 189
 Kewley L., Groves B., Kauffmann G., Heckman T., 2006, *MNRAS*, 372, 961
 King A., 2003, *ApJ*, 596, L27
 Lacy M., Laurent-Muehleisen S. A., Ridgway S. E., Becker R. H., White R. L., 2011, *ApJ*, 551, L17
 Laing R. A., Jenkins C. R., Wall J. V., Unger S. W., 1994, in Bicknell G. V., Dopita M. A., Quinn P. J., eds, *ASP Conf. Ser. Vol. 54, The First Stromlo Symposium: The Physics of Active Galaxies*. Astron. Soc. Pac., San Francisco, p. 201
 Lal D. V., Ho L. C., 2010, *A&A*, 139, 1089

- Liu G., Zakamska N. L., Greene J. E., Nesvadba N., Liu X., 2013, *MNRAS*, 436, 2576
- Lu N. et al., 2014, *ApJ*, 787, L23
- McCarthy P. J., Baum S. A., Spinrad H., 1996, *ApJS*, 106, 281
- McConnell N. J., Ma C. P., 2013, *ApJ*, 764, 184
- McElroy R., Croom S., Pracy M., Sharp R., Ho I. T., Medling A., 2015, *MNRAS*, 446, 2186
- McMullin J. P., Waters B., Schiebel D., Young W., Golap K., 2007, in Shaw R. A., Hill F., Bell D. J., eds, *ASP Conf. Ser. Vol. 376, Astronomical Data Analysis Software and Systems XVI*. Astron. Soc. Pac., San Francisco, p. 127
- Mathews W. G., Baker J. C., 1971, *ApJ*, 170, 241
- Mauch T., Sadler M. S., 2007, *MNRAS*, 375, 931
- Mendel J. T., Simard L., Palmer M., Ellison S. Patton D., 2014, *ApJS*, 210, 3
- Morganti R., Tadhunter C. N., Oosterloo T. A., 2005, *A&A*, 444, 9
- Mukherjee D., Bicknell G. V., Sutherland R., Wagner A., 2016, *MNRAS*, 461, 967
- Mullaney J. R., Alexandeer D. M., Fine S., Goulding A. D., Harrison C. M., Hickox R. C., 2013, *MNRAS*, 433, 622
- Narayan R., Yi I., 1994, *ApJ*, 428, L13
- Nesvadba N. P. H., Lehnert M. D., Eisenhauer F., Gilbert A., Tecza M., Abuter R., 2006, *ApJ*, 650, 693
- Nesvadba N. P. H., Lehnert M. D., De Breuck C., Gilbert A. M., van Breugel W., 2008, *A&A*, 491, 407
- Nims J., Quataert E., Faucher-Giguère C. A., 2015, *MNRAS*, 447, 3612
- Ochsenbein F., Bauer P., Marcout J., 2000, *A&AS*, 143, 23
- Osterbrock D. E., 1989, *Astrophysics of Gaseous Nebulae and Active Galactic Nuclei*. University Science Books, Mill Valley, CA
- Page M. J. et al., 2012, *Nature*, 485, 213
- Parma P., Murgia M., Morganti R., Capetti A., de Ruiter H. R., Fanti R., 1999, *A&A*, 344, 7
- Pearson C. et al., 2016, *ApJSS*, 227, 9
- Proga D., 2007, in Ho L. C., Wang J.-W., eds, *ASP Conf. Ser. Vol. 373, The Central Engine of Active Galactic Nuclei*. Astron. Soc. Pac., San Francisco, p. 267
- Quinn P., 1984, *ApJ*, 279, 596
- Ramos Almeida C., Piqueras López J., Villar Martín M., Bessiere P., 2017, *MNRAS*, 470, 964
- Reyes R. et al., 2008, *AJ*, 136, 2373
- Rupke D. S., Veilleux S., Sanders D. B., 2002, *ApJ*, 570, 588
- Sanders D. B., Mirabel I. F., 1996, *ARA&A*, 34, 749
- Sijacki D., Springel V., 2006, *MNRAS*, 371, 1025
- Sikora M., Stasińska G., Koziel-Wierzbowska D., Madejski G. M., Asari N. V., 2013, *ApJ*, 765, 62
- Silk J., Mamon G., 2012, *Res. Astron. Astrophys.*, 12, 917
- Silk J., Rees M., 1998, *A&A*, 331, L1
- Simard L., Mendel J., Trevor P., David R., Ellison S., McConnachie A., 2011, *ApJS*, 196, 11
- Solórzano-Iñarrea C., Tadhunter C. N., Axon D. J., 2002, *MNRAS*, 323, 965
- Stern J., Laor A., 2012, *MNRAS*, 426, 2703
- Stern J., Laor A., Baskin A., 2014, *MNRAS*, 438, 901
- Struck C., 1999, *Phys. Rep.*, 321, 1
- Tadhunter C., Shaw M., Clark N., Morganti R., 1994, *A&A*, 288, L21
- Tadhunter C. N., Morganti R., Robinson A., Dickson R., Villar Martín M., Fosbury R. A. E., 1998, *MNRAS*, 298, 1035
- Tadhunter C. N., Villa -Martín M., Morganti R., Bland-Hawthorn J., Axon D., 2000, *MNRAS*, 314, 849
- Tadhunter C., Morganti R., Rose M., Oonk J. B. R., Oosterloo T., 2014, *Nature* 511, 440
- Tumlinson J., Peebles M., Werk J., 2017, *ARA&A*, 55, 389
- Villar Martín M., Tadhunter C., Morganti R., Axon D., Koekemoer A., 1999, *MNRAS*, 307, 24
- Villar Martín M., Vernet J., di Serego Alighieri S., Fosbury R., Humphrey A., Pentericci L., 2003, *MNRAS*, 346, 273
- Villar Martín M., Humphrey A., González Delgado R., Colina L., Arribas S., 2011, *MNRAS*, 418, 2032
- Villar Martín M., Emonts B., Humphrey A., Cabrera Lavers A., Binette L., 2014, *MNRAS*, 440, 3202 (VM14)
- Villar Martín M., Bellocchi E., Stern J., Tadhunter C., González Delgado R., 2015, *MNRAS*, 454, 439
- Villar Martín M., Arribas S., Emonts B., Humphrey A., Tadhunter C., Bessiere P., Cabrera Lavers A., Ramos Almeida C., 2016, *MNRAS*, 460, 130
- Whittle M., 1985, *MNRAS*, 213, 33
- Whittle M., 1992a, *ApJS*, 79, 49
- Whittle M., 1992b, *ApJ*, 387, 109
- Wilson A. S., Ulvestad J. S., 1983, *ApJ*, 275, 8
- Woo J. H., Urry C. M., 2002, *ApJ*, 579, 530
- Woo J. H., Son D., Bae H. J., 2017, *ApJ*, 839, 120
- Xu C., Livio M., Baum S., 1999, *AJ*, 118, 1169
- York D. G. et al., 2000, *AJ*, 120, 1579
- Zakamska N., Greene J., 2014, *MNRAS*, 442, 784
- Zakamska N. L. et al., 2003, *AJ*, 126, 2125
- Zubovas K., King A., 2012, *ApJ*, 745, L34
- Zubovas K., King A., 2014, *MNRAS*, 439, 400

This paper has been typeset from a $\text{\TeX}/\text{\LaTeX}$ file prepared by the author.